Bioactive Materials 47 (2025) 295–312

Contents lists available at ScienceDirect

Bioactive Materials

journal homepage: www.keaipublishing.com/en/journals/bioactive-materials

An ultrasound-driven PLGA/Zn-KNN hybrid piezoelectric scaffold with direct and immunoregulatory antibacterial activity for bone infection

Yuhao Zheng [a], Shu Wang [b], Wenhe Jin [a], Zhuoxuan Li [c], Guoju Yang [d], Xiaoxu Li [a], Ning Li [a], Yue Wang [a], Fan Sheng [e,**], Zhiming Song [a,*]

[a] Department of Sports Medicine, Orthopaedics Clinic, The First Hospital of Jilin University, Changchun, 130021, Jilin, PR China
[b] Department of Radiotherapy, The Second Hospital of Jilin University, Changchun, 130041, Jilin, PR China
[c] Department of Orthopedic Surgery, The Second Hospital of Jilin University, Changchun, 130000, Jilin, PR China
[d] State Key Laboratory of Inorganic Synthesis & Preparative Chemistry, College of Chemistry, Jilin University, Changchun, 130012, Jilin, PR China
[e] Department of Dermatology, The Second Hospital of Jilin University, Changchun, 130041, Jilin, PR China

ARTICLE INFO

Keywords:
Ultrasound
Piezoelectric scaffold
Immunoregulatory antibacterial
Bone
Infection

ABSTRACT

Antibacterial piezoelectric materials have broad application prospects in the medical field because of their broad-spectrum antibacterial properties and no bacterial drug resistance. At present, one of the main problems in the application of piezoelectric materials is the low electrocatalytic efficiency, which limits its application in antibacterial field. In this study, a piezoelectric antibacterial (PLGA/Zn-KNN) scaffold was fabricated by incorporating zinc oxide (ZnO) into potassium-sodium niobate (KNN) and composited with a poly (lactic-co-glycolic acid) (PLGA) to achieve multicombination antibacterial for bone infection. The physicochemical properties of piezoelectric antibacterial scaffolds were analyzed. Bacterial, cell, and animal experiments were performed to characterize the antibacterial and infection treatment capabilities of piezoelectric scaffolds. The piezoelectric properties of the PLGA/Zn-KNN scaffold were enhanced by embedding ZnO particles into the KNN solid solution matrix. Furthermore, the piezoelectric scaffold released zinc ions, and electrical stimulation driven by ultrasound resulted in significant antibacterial effects through direct and immunoregulatory antibacterial pathways. Mechanistic investigation suggested that extracellular matrix ligands and complement and coagulation cascades may have a moderate effect on macrophage phagocytosis. This work highlights potential application methods for fabricating novel antibacterial hybrid piezoelectric scaffolds and engineering macrophages with immunoregulatory antibacterial activity.

1. Introduction

Bone infection is emerging as a global economic and health challenge, that leads to bone and surrounding soft tissue destruction, implant failure, and even a systemic inflammatory response [1,2]. Antibiotic administration is a major clinical approach for infection treatment [3]. However, its long-term use causes gut microbiota disturbance, bacterial evolution, gastrointestinal discomfort, and abnormal liver and kidney function [4]. Furthermore, antibiotic resistance and chronic inflammation can occur once bacterial biofilm forms in the host, which is exceedingly difficult to cure [5]. Hence, novel biomaterials and antimicrobial strategies for alternate antimicrobial therapeutics are desperately needed [6,7].

Recently, studies have attempted to identify effective non-antimicrobial treatments [8]. Physical stimulation is a promising antimicrobial therapy for destroying microbial structure via mechanical stretching or disturbing metabolism [1,9]. It can not only reduce microbial resistance but also kill drug-resistant bacteria [10,11]. Piezoelectric materials are biofriendly and exhibit good piezoelectric effects, which can form a built-in electric field and surface potential under external mechanical stress stimulation [12]. Moreover, researchers have found that exogenous ultrasonic waves can promote piezoelectric effect [13]. Hence, piezoelectric materials driven by ultrasonic activation are promising novel antibacterial methods that integrate both electrical and sonodynamic treatments. At present, the most widely available piezoelectric materials primarily contain piezoelectric crystals, piezoelectric

* Corresponding author.
** Corresponding author.
E-mail addresses: sfan0428@jlu.edu.cn (F. Sheng), zmsong@jlu.edu.cn (Z. Song).

https://doi.org/10.1016/j.bioactmat.2025.01.026
Received 1 October 2024; Received in revised form 2 January 2025; Accepted 21 January 2025
2452-199X/© 2025 The Authors. Publishing services by Elsevier B.V. on behalf of KeAi Communications Co. Ltd. This is an open access article under the CC BY-NC-ND license (http://creativecommons.org/licenses/by-nc-nd/4.0/).

ceramics, and organic piezoelectric materials [14]. Zhu et al. designed piezoelectric barium titanate with antibacterial drugs and self-assembled MOFs, which exhibited synergistic antibacterial efficacy via ROS generation induced by sonodynamic processes and drug release [15]. Zhang et al. prepared sulfur-doped graphdiyne nanosheets with peroxidase-like activity enhanced by the piezoelectric effect for bacterial disinfection [16]. Nevertheless, the existing piezoelectric materials suffer from many issues, such as nonbiodegradation or toxicity. Furthermore, there are still many issues with electrical stimulation, including high energy consumption, low bacteria-killing efficacy, and safety issues [17]. Potassium-sodium niobate ($K_{0.5}Na_{0.5}NbO_3$, KNN) possesses piezoelectric characteristic, biocompatibility, and biodegradation, but it lacks antimicrobial properties [18]. Hence, the preparation of KNN with antibacterial efficacy is an intriguing solution for non-antimicrobial treatment.

Many metal-based nanomaterials and metal ions, such as silver ions (Ag^+), magnesium ions (Mg^{2+}), copper ions (Cu^{2+}), and zinc ions (Zn^{2+}), have exhibited outstanding antimicrobial effects by inducing bacterial cell membrane disruption, oxidative stress, and intracellular biomolecule disruption [19]. Nevertheless, these effects are dose-dependent. Excessive free ions result in cytotoxicity and even severe damage to organisms. Zinc oxide nanomaterials have been widely studied for their antibacterial properties. They play an antibacterial role mainly through two mechanisms [20]: direct contact with bacteria and non-contact antibacterial mechanism. One of the non-contact mechanisms is the release of Zn^{2+} ions, which can attach to the surface of bacterial cell wall, destroy the permeability of bacterial cell membrane and affect the metabolism of amino acids. The introduction of ZnO dopant into KNN-based piezoelectric ceramics can enhance the lattice distortion of BO6 octahedron, thus enhancing the piezoelectric properties, including enhancing piezoelectric coefficient (kp), piezoelectric charge constant (d33) and Curie temperature (Tc) [21]. Therefore,

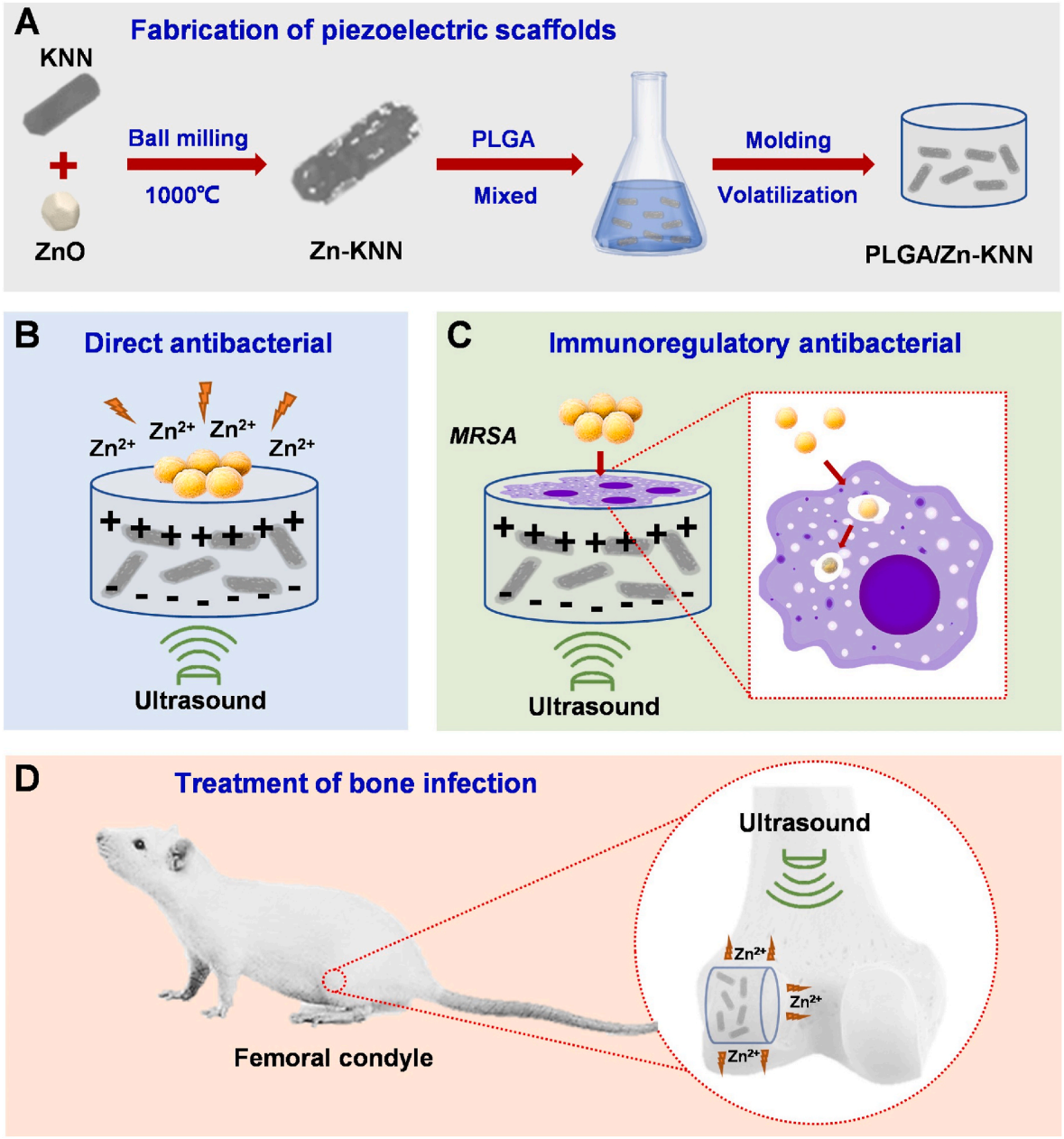

Fig. 1. An ultrasound-driven PLGA/Zn-KNN hybrid piezoelectric scaffold promotes bone infection. (A) The synthesis and fabrication processes of the PLGA/Zn-KNN hybrid piezoelectric scaffold; (B) Direct antibacterial effect by releasing ions and generating electricity; (C) Indirect antibacterial effect by regulating M1 macrophages (D) Ultrasound-driven PLGA/Zn-KNN hybrid piezoelectric scaffold treating bone infection in SD rats.

adjusting the phase transition temperature of KNN piezoelectric ceramics by adding ZnO maybe an effective way to obtain antibacterial and piezoelectric properties. However, there is currently a lack of research on the antibacterial properties and mechanisms of piezoelectric materials combined with ZnO.

In this study, a piezoelectric antibacterial composite material (Zn-KNN) was synthesized, in which nanosized ZnO particles were embedded in a $K_{0.5}Na_{0.5}NbO_3$ solid solution matrix. The crystal structure and physicochemical properties of Zn-KNN were investigated systematically. Furthermore, the piezoelectric antibacterial scaffolds were prepared by PLGA incorporated with Zn-KNN particles. The PLGA/Zn-KNN piezoelectric scaffold released zinc ions, and electrical stimulation driven by ultrasound resulted in significant antibacterial effects through direct and immunoregulatory antibacterial pathways. Upon proper US irradiation, the PLGA/Zn-KNN piezoelectric scaffold can realize the rapid degradation and maintain bone metabolic homeostasis for bone infection in a rat model. Based on RNA sequencing, the possible molecular mechanisms are that PLGA/Zn-KNN + may activate Laminin-integrin signaling pathway mediated complement and coagulation cascades, and then indirectly activated M1 macrophage phenotype-related signaling pathway, which digested and ingested bacteria under phagocytosis (see Fig. 1).

2. Results

2.1. Characterization of the piezoelectric scaffolds

The size and morphology of the as obtained KNN and Zn-KNN particles were characterized by SEM (Fig. 2A and B). The crystal length of KNN particles is about 1∼20 μm. Under the same synthesis conditions, the crystal length of Zn-KNN particles is about 1∼10 μm. The detailed element distributions recorded from the same area are provided (Fig. 2C). The elements of K, Na, Nb, and Zn occupy the same areas, while the distribution of partial Zn is isolated (indicated by the white arrow). The isolated partial Zn was further analyzed by HRTEM micrographs and selected area diffraction patterns. The (002) interplanar spacing of the KNN particles is about 0.3948 nm (Fig. 2D). Under the same synthesis conditions,the (002) interplanar spacing of Zn-KNN particles is about 0.4120 μm (Fig. 2E). The isolated partial Zn is adsorbed on the surface of the grain boundaries of Zn-KNN in the form of nano ZnO (Fig. 2E). The electron diffraction patterns indicate that KNN and Zn-KNN particles have the same crystal structure (Fig. 2F). The results were further confirmed by XRD. Fig. 2G shows the XRD patterns of the KNN particles. The diffraction peaks of the KNN particles (PDF#77-0038) are assigned to (002), (022), (400), (204), (422), and (440). The diffraction peaks of the ZnO particles (PDF#76–0704) are assigned to (100), (002), (101), (102), and (103). The above results confirm the composite structure of KNN and ZnO. It could expect that ZnO exists in two forms. Some Zn randomly distributes in the KNN matrix, which increase its interplanar spacing. The other part of ZnO could be adsorbed on the grain boundaries of KNN, which could act as the role of sintering aid.

As shown in Fig. 3A, a piezoelectric scaffold was fabricated by doping PDA-modified piezoelectric KNN or Zn-KNN particles into PLGA. The KNN or Zn-KNN particles distributed in the piezoelectric scaffold were also confirmed by element mapping of K, Na, Nb, and Zn in SEM characterization (Fig. 3B). The FTIR spectra of the piezoelectric scaffolds are displayed in Fig. 3C. The band at 1164 cm^{-1} (C-O-C stretching), 1721 cm^{-1} (C=O stretching), 2867 cm^{-1} (CH_2 stretching), and 2946 cm^{-1} (CH_3 stretching) can be ascribed to the PLGA characteristic peak. Fig. 3D shows the concentration of released Zn^{2+} and Nb^{5+} in the supernatant collected at 1–12 days. Zn^{2+} and Nb^{5+} was released less in the first 6 days, reaching up to 0.4 and 0.8 mg/L respectively. The concentration of released Zn^{2+} is between 0.4 and 0.6 mg/L after 6 days. The concentration of released Nb^{5+} is between 0.8 and 1.0 0.01 mg/L after 6 days. The sustained releasing of Zn^{2+} and Nb^{5+} clearly indicates the dissolving of KNN and Zn-KNN in saline solution. To measure the electrical output of the piezoelectric scaffold upon US excitation, the drive signal for US (frequency 1 MHz) was set as a pulse width of 1 ms and a pulse interval of 0.5 s. The open-circuit voltage generated by PLGA/KNN scaffolds under US excitation was 20 mV (Fig. 3E–F). The open-circuit voltage generated by PLGA/Zn-KNN scaffolds under US excitation was 40 mV (Fig. 3G–H). Therefore, the incorporation of ZnO in KNN can greatly enhance piezoelectric properties, which were compared by using the VASP (Tables S1–S2). Piezoelectric constant of PLGA/Zn-KNN scaffolds is higher than that of PLGA/KNN in simulated environments with different shear force directions and crystal polarization directions (Fig. 3I), which can be maintained after soaked in PBS for 14days (Fig. S1).

2.2. Cytocompatibility and osteogenic properties of the piezoelectric scaffolds

The CCK-8 assay was performed and shown in Fig. S2 to probe the effect of PLGA/KNN and PLGA/Zn-KNN scaffolds and ultrasound ($^+$) on bone marrow mesenchymal stem cells (BMSCs) proliferation. Our data indicated that PLGA/KNN and PLGA/Zn-KNN scaffolds and ultrasound ($^+$) showed no effect on the activity of BMSCs. BMSCs treated for 3 days with PLGA/KNN and PLGA/Zn-KNN scaffolds and ultrasound ($^+$) were stained with TRITC phalloidin and DAPI to show the cytoskeleton and cellular nuclei respectively. The results, shown in Fig. 4A, revealed that the BMSCs spread smoothly and maintained a normal shape treated with PLGA/KNN and PLGA/Zn-KNN scaffolds and ultrasound ($^+$) for 2 days. Live/Dead staining of the BMSCs co-culture with PLGA/KNN and PLGA/Zn-KNN scaffolds and ultrasound ($^+$) groups grew to the entire area, while the number of dead cells were not found (Fig. 4B). Whereafter, the early marker of osteogenic differentiation was assessed by the alkaline phosphatase (ALP) staining. The results in Fig. 4C were significantly enhanced with the addition of PLGA/KNN or PLGA/Zn-KNN scaffolds and ultrasound ($^+$). At the same time, the relative gene expression of osteoclast marker genes OPN, OCN and Col-1 of BMSCs incubated with PLGA/KNN or PLGA/Zn-KNN scaffolds and ultrasound ($^+$) for 14 days exhibited significantly up-regulated expression, implying that the scaffolds and ultrasound ($^+$) effect favored the osteogenic differentiation of BMSCs.

2.3. Direct antibacterial effect of releasing zinc ions and generating electricity

The inactivation effect of the piezoelectric scaffolds with and without ultrasonication on *E. coli and MRSA* was compared to that of the control without any scaffolds or ultrasonic treatment (Fig. 5A and B). CFU assay was used to evaluate bacterial inactivation to determine the number of viable cells remaining after treatment. The plate count is shown in Fig. 5C and D. There was no significant difference in the number of colonies between the PLGA/KNN group and the control group. The number of colonies in the PLGA/Zn-KNN group was significantly lower than that in the control group and the PLGA/KNN treatment group. The number of colonies in the PLGA/Zn-KNN synergistic ultrasound treatment group was significantly lower than that in the PLGA/Zn-KNN treatment group alone. Pure PLGA/KNN had no antibacterial ability, but ultrasound treatment made it have antibacterial properties. The PLGA/Zn-KNN group has antibacterial ability after introducing ZnO nanoparticles, and ultrasound treatment further enhanced the antibacterial ability of the PLGA/Zn-KNN. Fig. 5E shows that after the PLGA/Zn-KNN combined with ultrasound treatment, the OD values of *E. coli and MRSA* were decreasing sharply, which was consistent with the previous data. Fig. 5F shows that *E. coli and MRSA* in the control group and PLGA/KNN group emitted green fluorescence, indicating that all the bacterial were living cells. After treatment with the ZnO and PLGA/Zn-KNN, a small number of bacterial were stained red, which suggested that the PLGA/Zn-KNN changed in bactericidal effects. After PLGA/Zn-KNN

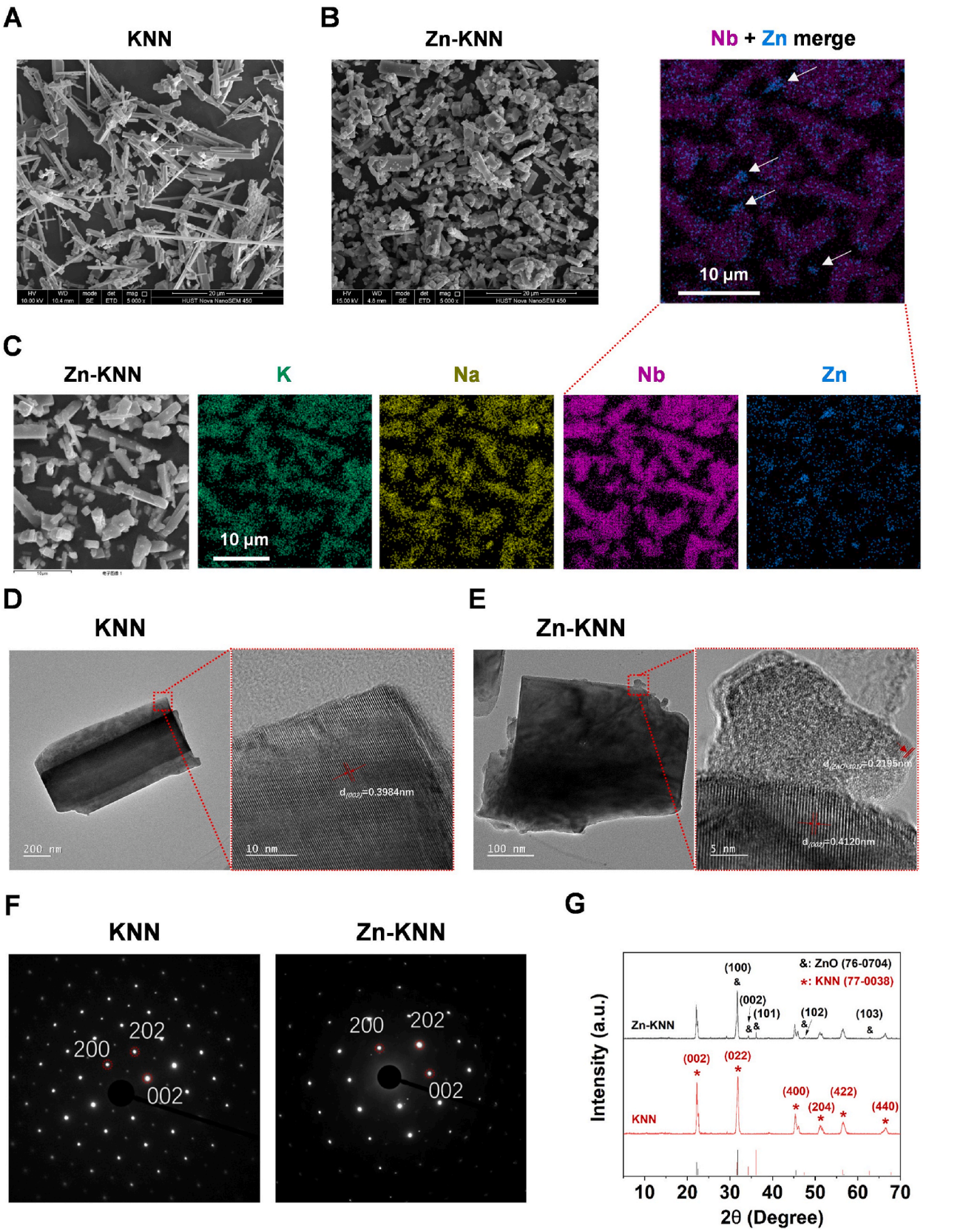

Fig. 2. Characterization of KNN and Zn-KNN particles. (A) SEM images of KNN particles; (B) SEM images of Zn-KNN particles; (C) EDS elemental mapping of Zn-KNN particles; (D) HRTEM image of KNN particles; (E) HRTEM image of Zn-KNN particles; (F) The spot on the electron diffraction of KNN and Zn-KNN particles; (G) The XRD pattern of KNN and Zn-KNN particles.

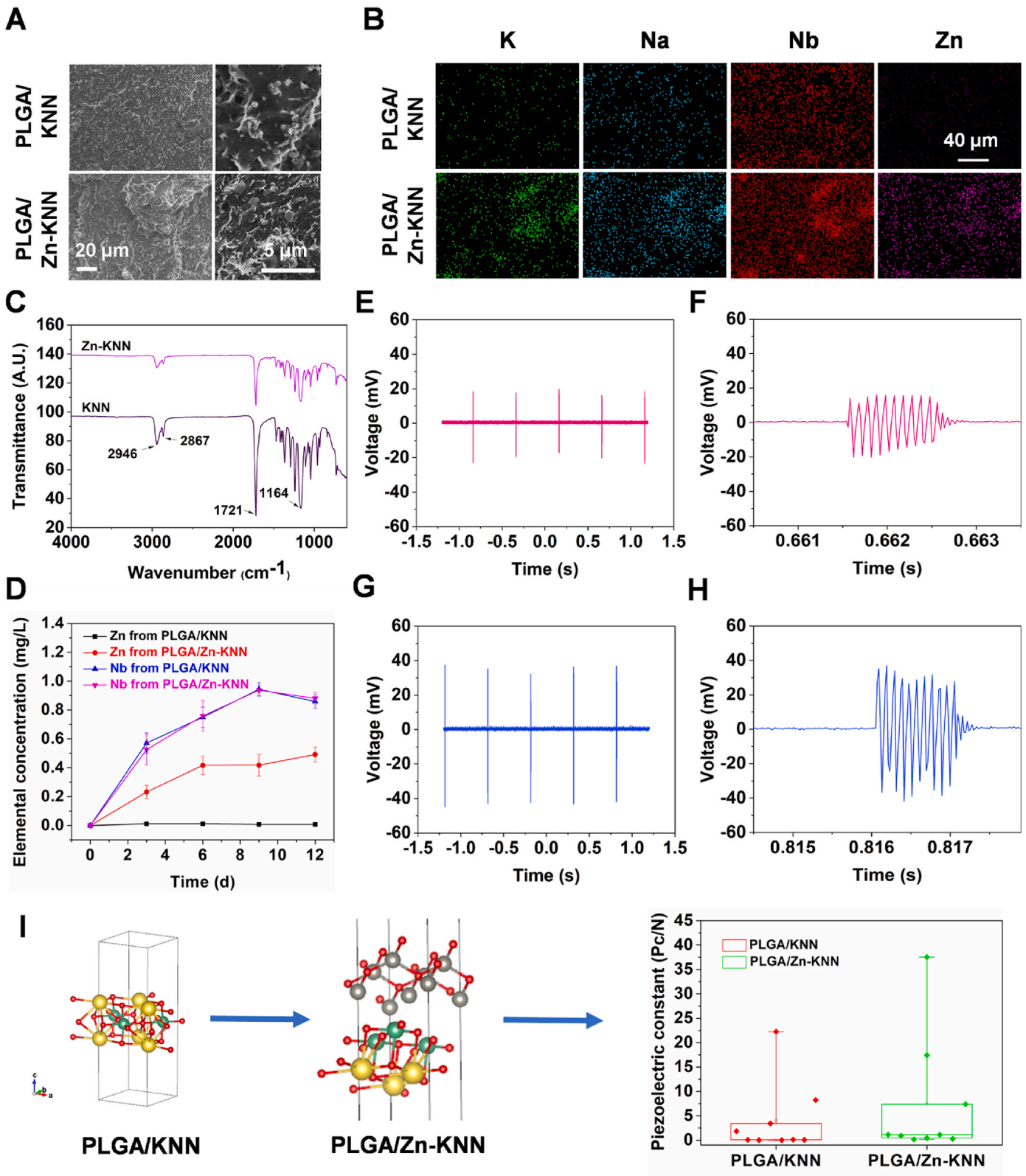

Fig. 3. Characterization of the piezoelectric scaffolds. (A–B) SEM images and EDS elemental mapping of PLGA/KNN and PLGA/Zn-KNN scaffolds; (C) FTIR of PLGA/KNN and PLGA/Zn-KNN scaffolds; (D) Ion concentrations in the saline solution after soaking with PLGA/KNN and PLGA/Zn-KNN scaffolds for different times (n = 3); (E–F) The open-circuit voltage generated by PLGA/KNN scaffolds under US excitation (frequency 1 MHz, pulse width 1 ms, pulse interval 0.5 s); (G–H) The open-circuit voltage generated by PLGA/Zn-KNN scaffolds under US excitation (frequency 1 MHz, pulse width 1 ms, pulse interval 0.5 s); (H) Piezoelectric constant of PLGA/KNN and PLGA/Zn-KNN scaffolds in simulated environments with different shear force directions and crystal polarization directions.

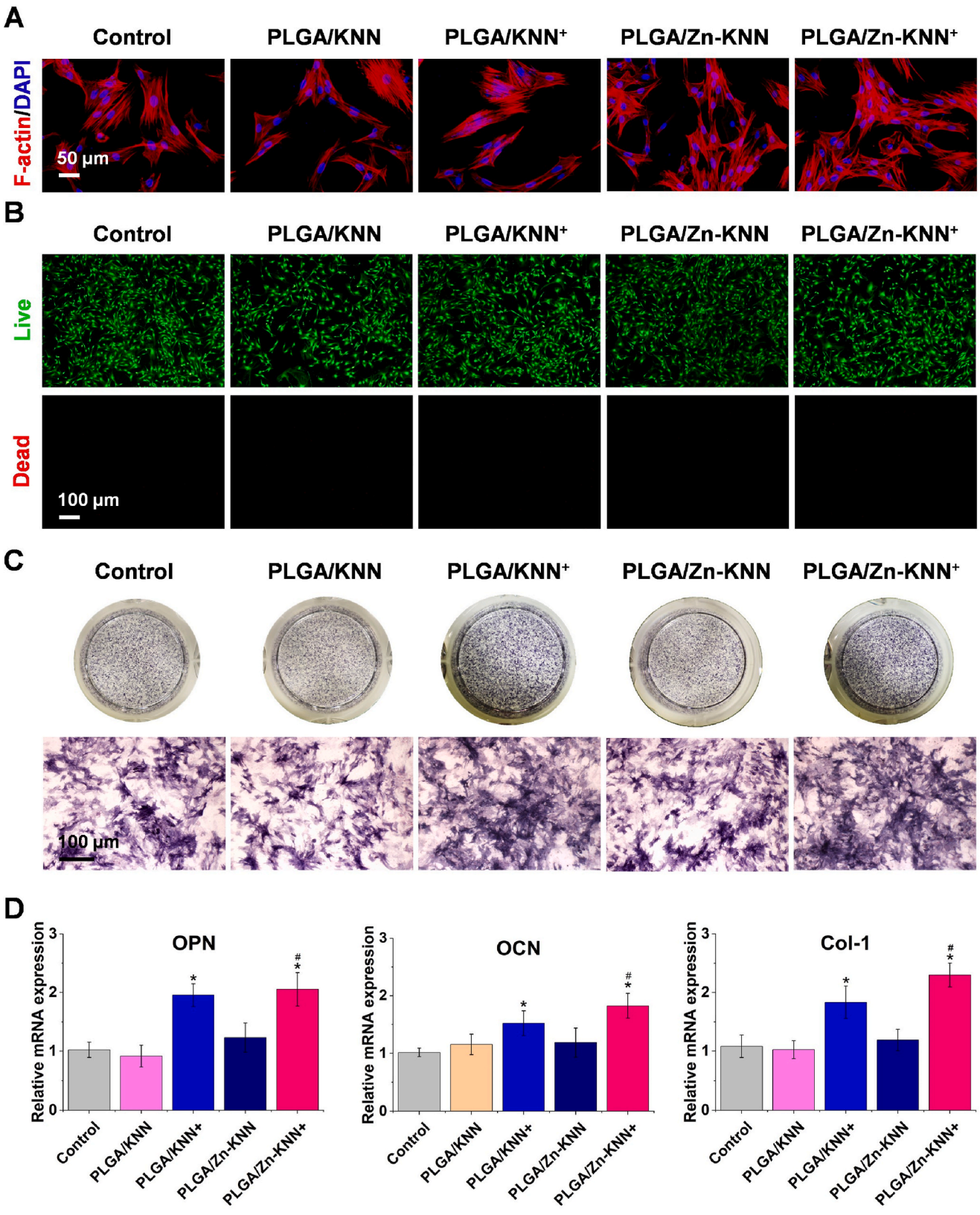

Fig. 4. Cytocompatibility and osteogenic properties of the piezoelectric scaffolds. (A) F-actin and nuclear staining were conducted to probe the effect of PLGA/KNN and PLGA/Zn-KNN scaffolds and ultrasound (+) on the function of BMSCs; (B) Live-dead cell staining of BMSCs incubated with PLGA/KNN and PLGA/Zn-KNN scaffolds and ultrasound (+) for 24 h; C) ALP staining was performed to evaluate the effect of PLGA/KNN and PLGA/Zn-KNN scaffolds and ultrasound (+) on the osteogenic differentiation of BMSCs; D) Relative gene expression of osteoclast marker genes OPN, OCN and Col-1 of BMSCs incubated with PLGA/KNN and PLGA/Zn-KNN scaffolds and ultrasound (+) for 14 days.

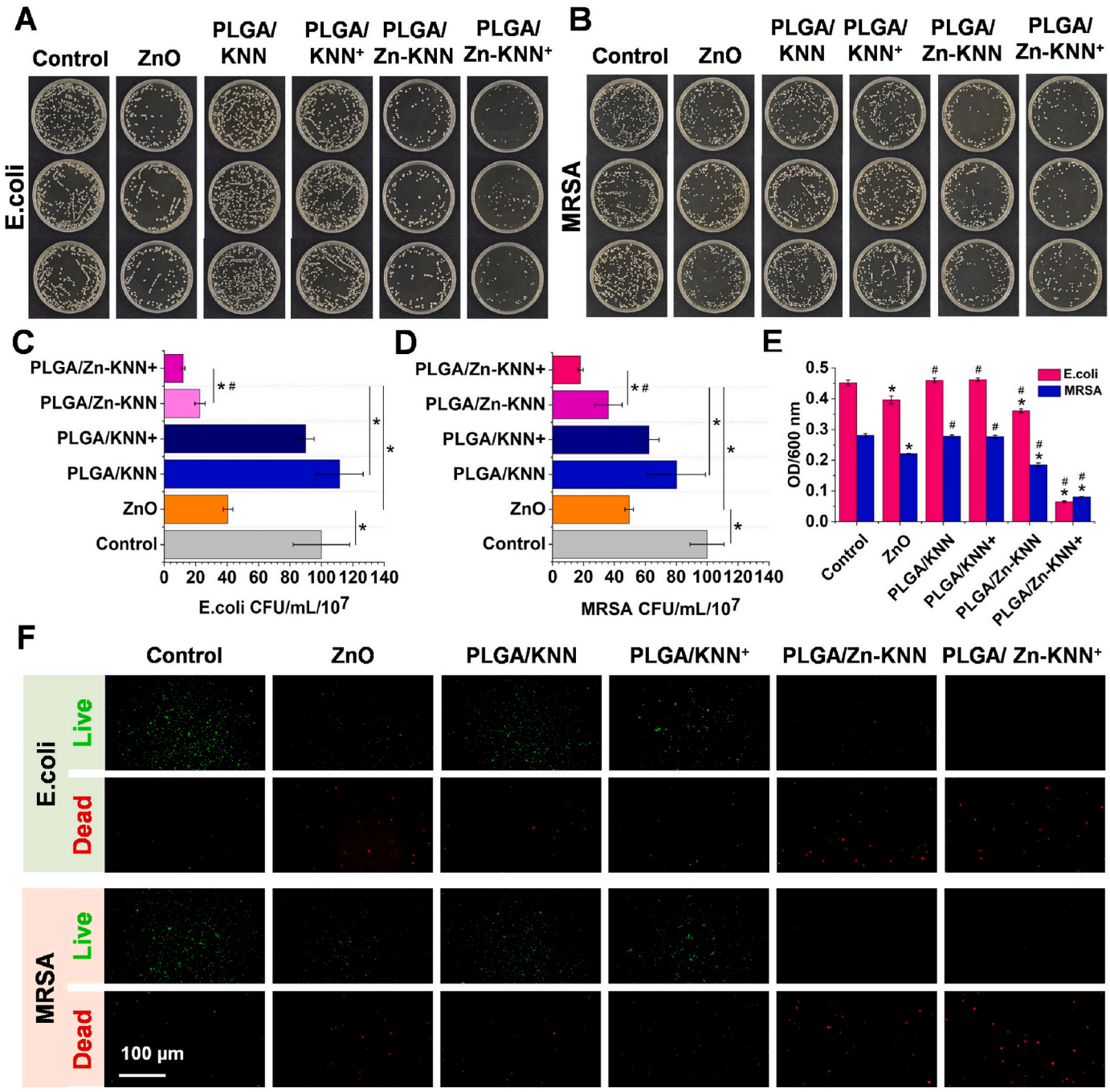

Fig. 5. Direct antibacterial effect of the piezoelectric scaffolds with ultrasound exposure. (A–B) Viable colonies on standard agar plates after *E. coli and MRSA* treated with various scaffolds and ultrasound ($^+$); (C–D) Bacterial colony count of *E. coli and MRSA*; (E) OD value of bacteria treated with various scaffolds and ultrasound ($^+$); (F) Live/dead staining assay of bacteria treated with various scaffolds and ultrasound ($^+$).

combined with ultrasound treatment, the proportion of bacterial stained red significantly increased, demonstrating that PLGA/Zn-KNN combined with ultrasound treatment significantly improved the bactericidal effects on *E. coli and MRSA*.

2.4. Indirect antibacterial effect of regulating macrophage phagocytosis

The phagocytosed *MRSA* in the macrophages was observed by fluorescence staining. Fig. 6A shows that the phagocytosed *MRSA* cells were stained green, and the macrophage nucleus was stained blue. Obviously, the PLGA/Zn-KNN scaffolds in the ultrasound ($^+$) group exhibited more *MRSA* phagocytosis in macrophages than did the other groups. The fluorescence intensity increased in the order of Control, PLGA/KNN, PLGA/KNN$^+$, PLGA/Zn-KNN, and PLGA/Zn-KNN$^+$ (Fig. 6A), which suggested that most bacteria were engulfed by macrophages cultured on PLGA/Zn-KNN$^+$. Therefore, macrophages cultured on the PLGA/Zn-KNN $^+$ scaffolds exhibited the greatest ability to phagocytose *MRSA*. The phagocytosis of *MRSA* by macrophages was further determined by TEM. Fig. 6B illustrates that the PLGA/Zn-KNN scaffolds in the ultrasound ($^+$) group exhibited more phagocytosed *MRSA* in macrophages than did the other groups. The PLGA/Zn-KNN$^+$ scaffolds exerted the highest phagocytosis rate among the other groups. Immunofluorescence staining was performed to label the polarized macrophages (M1: TNF-α positive, CD86 positive). As demonstrated in Fig. 6C, the PLGA/Zn KNN scaffold

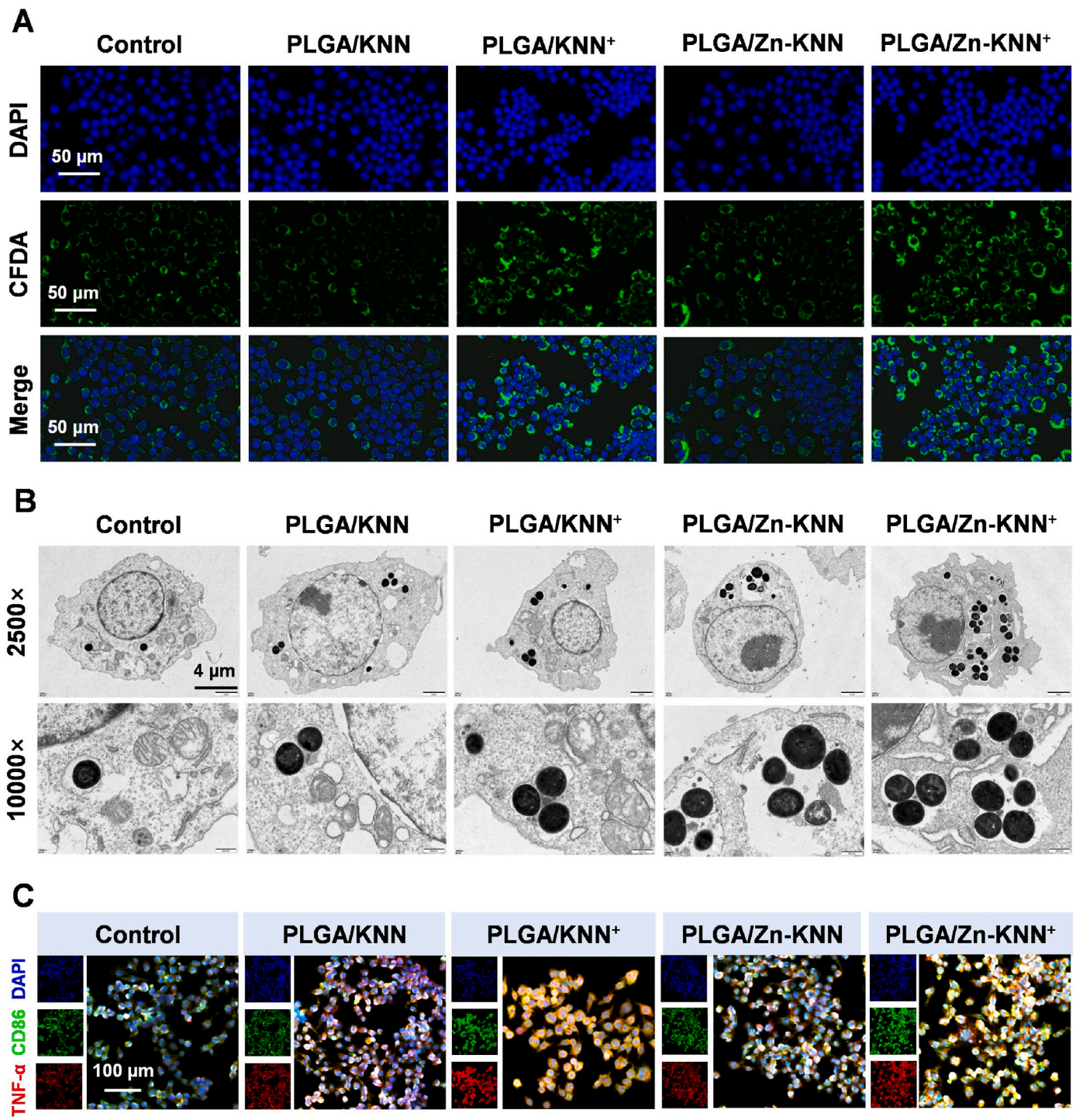

Fig. 6. Indirect antibacterial effect of the piezoelectric scaffolds with ultrasound exposure. (A) Macrophages treated with scaffolds and ultrasound ($^+$) could capture and deplete more CFDA-labeled *MRSA*; (B) TEM images of bacterial phagocytosis of macrophages treated with scaffolds and ultrasound ($^+$); (C) Immunofluorescence staining images of CD86 and TNF-α after treatment with PLGA/Zn-KNN scaffolds and ultrasound ($^+$) for 2 days.

combined with ultrasound treatment (PLGA/Zn-KNN$^+$) exerted the highest proportion of M1 polarized macrophages and inflammatory cytokines (TNF-α), suggesting that ultrasound-mediated electrical stimulation boosted the activation of M1 polarized macrophages and the secretion of cytokines, which may enhance the phagocytic effect of macrophages on bacteria.

2.5. Possible mechanism of piezoelectrically enhanced macrophage phagocytosis

The molecular mechanism underlying the effect of piezoelectric scaffold treatment on macrophages was determined via RNA sequencing. A total of 4065 differentially expressed genes (DEGs), including 2418 upregulated and 1647 downregulated genes, were obtained between the PLGA/KNN and control groups (Fig. 7A and B). A total of 3278 differentially expressed genes (DEGs), including 1995

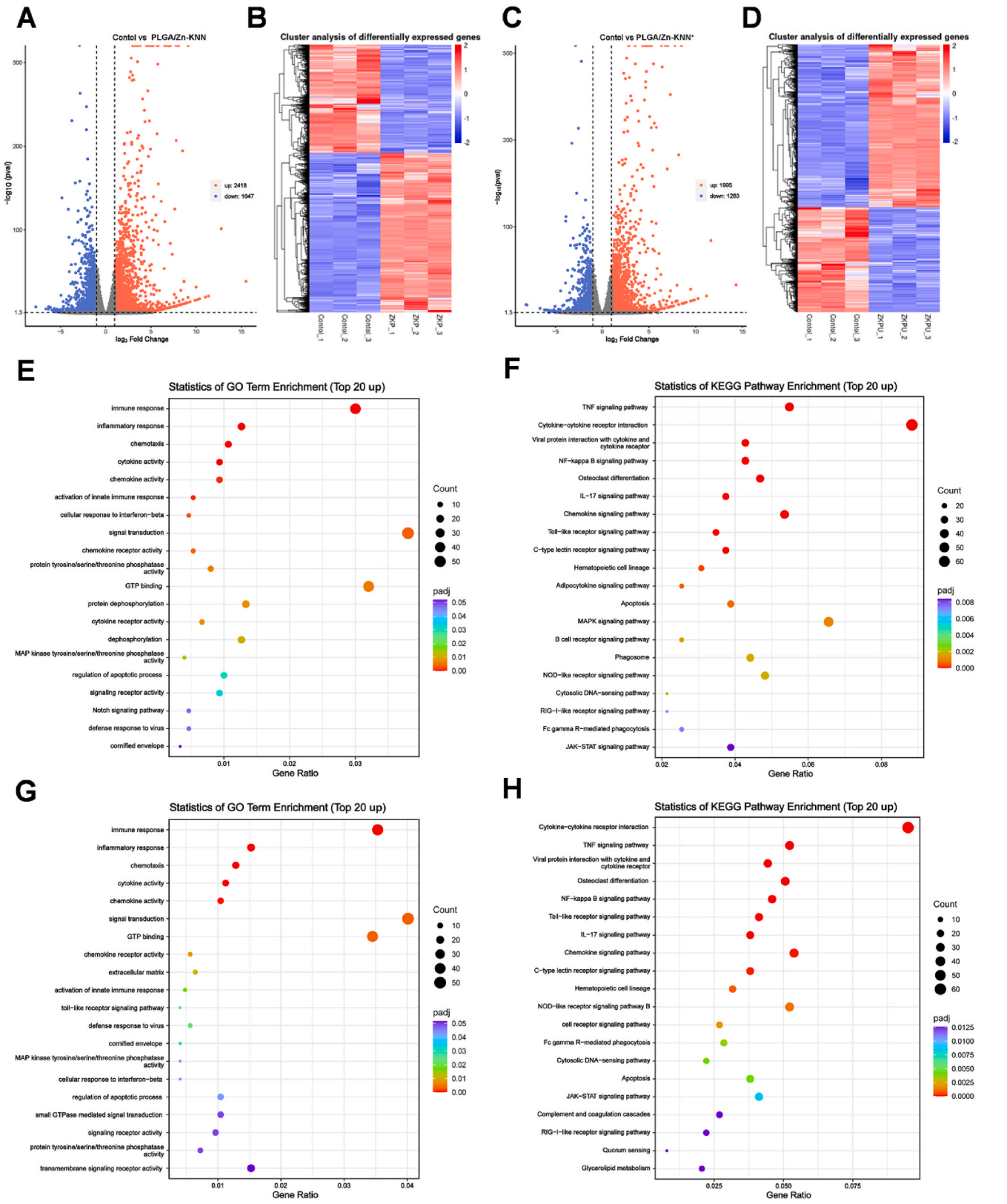

Fig. 7. Transcriptome quantitative analysis of piezoelectrically enhanced macrophage phagocytosis. (A) Volcano plot of DEGs between the control and PLGA/Zn-KNN groups; (B) Heatmap of DEGs between the control and PLGA/Zn-KNN groups; (C) Volcano plot of DEGs between the control and PLGA/Zn-KNN^{+} groups; (D) Heatmap of DEGs between the control and PLGA/Zn-KNN^{+} groups; (E) GO enrichment analysis of DEGs between the control and PLGA/Zn-KNN groups; (F) KEGG pathway enrichment analysis of upregulated DEGs between the control and PLGA/Zn-KNN groups; (G) GO enrichment analysis of upregulated DEGs between the control and PLGA/Zn-KNN^{+} groups; (H) KEGG pathway enrichment analysis of upregulated DEGs between the control and PLGA/Zn-KNN^{+} groups.

upregulated and 1283 downregulated genes, were identified between the PLGA/Zn-KNN$^+$ and the control groups (Fig. 7C and D). The GO functional enrichment analysis of DEGs between the PLGA/Zn-KNN or PLGA/Zn-KNN$^+$ and control groups was performed, as shown in Fig. 7E and G. Many of the significantly affected enriched GO terms (top 20) were related to immune response, inflammatory response, chemotaxis, cytokine activity, chemokine activity, etc. The KEGG analysis was used to identify signaling pathways that were significantly enriched in DEGs between the PLGA/Zn-KNN or PLGA/Zn-KNN + group and the control group (Fig. 7F and H) (Figs. S3 and S4). The KEGG pathway results demonstrated that immune-related signaling pathways, such as the TNF signaling pathway, cytokine-cytokine receptor interaction, viral protein interaction with cytokine and cytokine receptor, NF-kappa B signaling pathway, AMPK signaling pathway, and chemokine signaling pathway, were enriched.

To further explore the functions of macrophages, the GO functional enrichment analysis of DEGs between the PLGA/Zn-KNN$^+$ and PLGA/Zn-KNN groups was performed, as displayed in Fig. 8A. Many of the significantly enriched GO terms (top 20 up) were related to the extracellular region, myosin complex, motor activity, cytokine activity, inflammatory response, immune response, etc. The KEGG pathway results between the PLGA/Zn-KNN$^+$ and the PLGA/Zn-KNN groups (Fig. 8B) demonstrated that cytokine-cytokine receptor interaction and complement and coagulation cascades were overexpressed. Based on the KEGG analysis, the software cluster profiler (version 3.8.1) was used for Gesa analysis, and the GSEA results are visually displayed in the form of a network diagram (Fig. 8C and D). PLGA/Zn-KNN$^+$ mainly upregulated complement and coagulation cascades. According to the protein-protein interaction network (PPI network) results, the Lmab1 played a vital role in regulating macrophage immunological function.

2.6. *In vivo therapeutic efficacy of bone infection*

PLGA/Zn-KNN scaffolds exhibited excellent antibacterial properties after in vitro ultrasonic treatment, which prompted us to explore the potential in vivo effects. The infectious femoral condyle defect model is shown in Fig. S5. To further investigate the degradation process of the scaffolds in vivo and the formation of new bone, reconstructed 3D images of the left femur at 2 months are shown in Fig. 9A. Only a small amount of new bone formed appeared at the defect site in the PLGA/Zn-KNN$^+$ group. The obvious osteolysis and severe trabecular bone disorder indicate the successful establishment of typical bone infection, but there were still significant gaps at the defect site that were not repaired. In contrast, other groups showed milder symptoms of osteomyelitis and new bone formation, confirming the significance of pore structure in bone regeneration. In addition, rats treated with PLGA/Zn-KNN$^+$ had greater bone healing area (Fig. 9B) and degradation rates of the scaffold (Fig. 9C). The quantitative analysis in Fig. 9D confirmed that the BV/TV ratios in the PLGA/Zn-KNN$^+$ group were significantly greater than those in the other groups. In summary, the use of PLGA/Zn-KNN scaffolds and their acoustoelectric effect improved the microenvironment of osteomyelitis.

Gram staining is used to observe bacteria in tissues, among which dark (purple) is gram-positive bacteria and red is gram-negative bacteria. As shown in Fig. S6, in the control and PLGA/KNN groups, the defect sites were only filled with a large amount of deep purple areas. Nevertheless, the PLGA/Zn-KNN groups exhibited a small quantity of deep purple areas, and the PLGA/Zn-KNN$^+$ groups did not exhibit any deep purple areas. The main reason for this phenomenon is that ZnO in PLGA/Zn-KNN has certain antibacterial properties. It is worth noting that ultrasonic treatment even further stimulated the discharge of PLGA/Zn-KNN and enhanced its antibacterial properties. H&E and Massion staining were used to evaluate the effects of PLGA/Zn-KNN scaffolds and ultrasonic exposure on bone regeneration of the femur lateral condyle regions. As shown in Fig. 10A, the PLGA/Zn-KNN$^+$ group exhibited to more newly-formed bone, whereas the other groups possessed limited formed bone and fibrous tissues around the implant after 2 months. TRAP is a specific osteoclastic enzyme, and the TRAP staining was conducted to indicate the number and distribution of osteoclasts. As shown in Fig. 10B, the osteoclasts were stained in dark color. The combination of PLGA/Zn-KNN scaffolds and ultrasound ($^+$) significantly reduced the dark color, which suggested that osteoclast activity of the new bone tissues was suppressed in the PLGA/Zn-KNN$^+$ group. Immunofluorescence staining of osteocalcin (OCN, red) and osteopontin (OPN, green) proteins in different scaffold groups is shown in Fig. 10C. The OCN and OPN fluorescence intensity in the PLGA/Zn-KNN$^+$ group was significantly enhanced than the other groups, providing the desired regenerative microenvironment for bone infection.

3. Discussion

Bone infection and regeneration involve antibacterial and immunity. Their activities and interactions must be accurately adjusted to effectively heal after injury. Although great progress has been made in understanding the immune microenvironment process to control bone infection, it is still a challenge to effectively translate these mechanisms into clinical application [22–25]. In the present study, a novel PLGA/Zn-KNN piezoelectric scaffold was successfully constructed for treating bone infection. PLGA/Zn-KNN not only released zinc ions and generated electricity for direct antibacterial activity, but also indirectly regulated immunity for antibacterial in vitro experiments. Moreover, the key ionic and electrical stimulation signaling pathway were identified at the molecular level by transcriptome sequencing. Finally, in vivo experiments were conducted to verify the therapeutic effect on bone infection. Collectively, the results demonstrated that the ultrasound-driven PLGA/Zn-KNN piezoelectric scaffold regulated macrophage M1 polarization by creating an ionic and electrical environment, enhancing antibacterial activity, and ultimately facilitating the healing of bone infection.

The molten salt method is a simple preparation process, that can accurately control the morphology of the synthesized nanopowder and improve the performance of ceramics by adjusting the proportion of raw materials and ions or compounds [21,25]. Sodium potassium lithium niobate ($Na_{0.47}K_{0.47}Li_{0.06}NbO_3$) ceramics were prepared by adding ZnO via a high-energy ball milling process and sintering via a microwave technique. The SEM images displayed that the introduction of ZnO decreased the grain size of KNN. K, Na, and Nb occupied the same areas, while Zn was isolated. ZnO existed in two forms, some ZnO crystallizes in isolated nanosized particles that were randomly distributed in the KNN matrix, and the other part of the ZnO could filled in the grain boundaries of the KNN, to act as a sintering aid [26]. The XRD patterns and HRTEM images indicated that KNN crystallized into a single perovskite structure, while all Zn-KNN had a composite structure with two sets of diffraction peaks and lattice fringes of KNN and ZnO. To investigate the piezoelectric performance of KNN and Zn-KNN, PLGA/KNN and PLGA/Zn-KNN scaffolds were fabricated. The addition of ZnO enhanced open-circuit voltage and piezoelectric constant (d_{33}) [27]. The sustained release of Zn and Nb clearly indicated the dissolution of KNN and Zn-KNN in PBS solution.

ZnO can induce antibacterial activity through a variety of mechanisms, such as bacterial membrane rupture, reactive oxygen species production, and intracellular substance leakage [28]. The antibacterial action of ZnO nanoparticles includes three main mechanisms: (1) the production of ROS, (2) the release of Zn^{2+} ions, and (3) the interaction of nanoparticles with the cell wall [29]. Previous studies have reported various possible mechanisms of electro antibacterial activity, which can be classified as direct and indirect [30]. The former is caused by electrical stimulation leading to leakage of bacterial cell membranes, resulting in the loss of essential components within the cells and disruption of bacterial metabolic processes; the latter is related to the production of antibacterial components and changes in pH value. Electrical stimulation induces electrolytic reactions to produce toxic

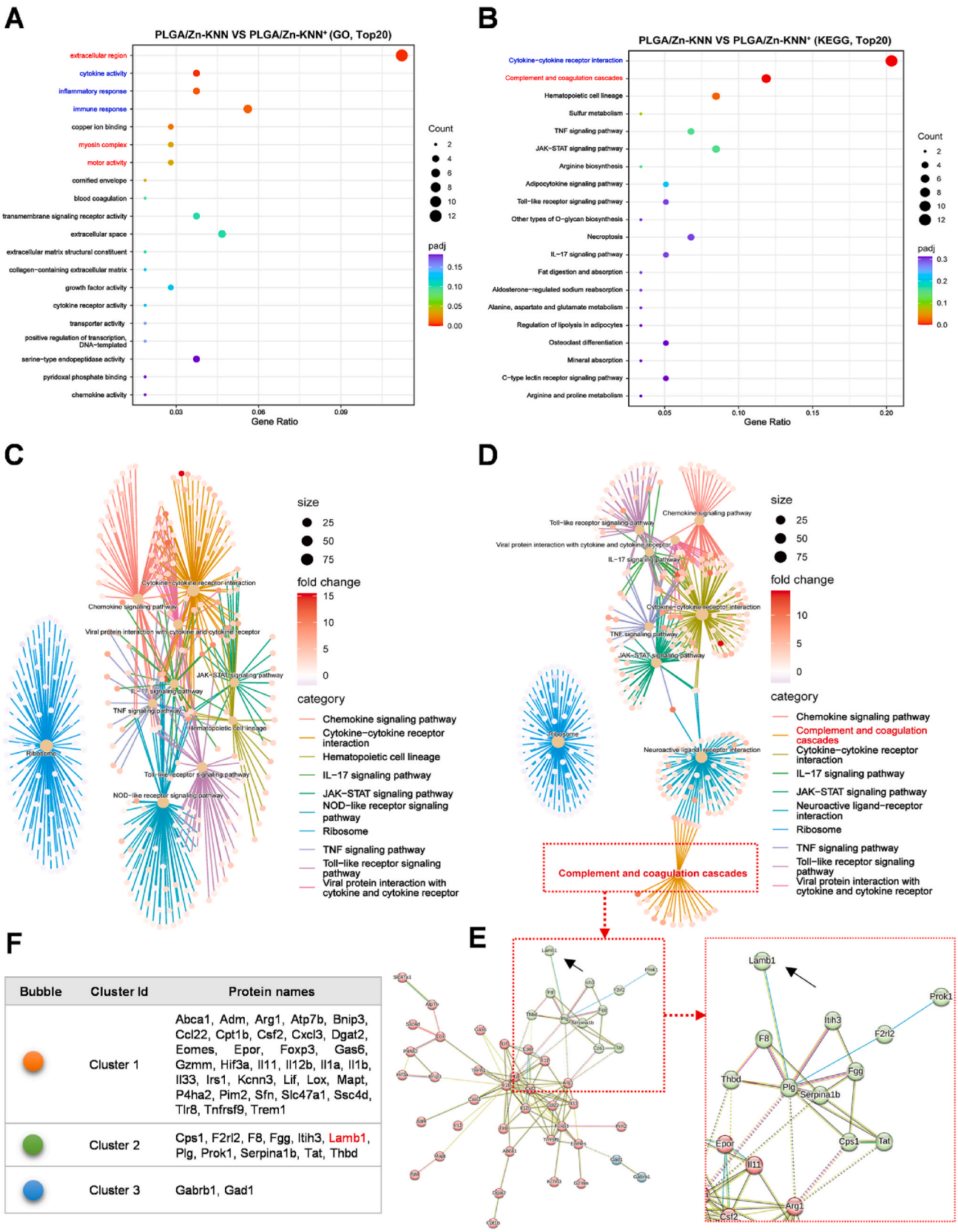

F

Bubble	Cluster Id	Protein names
	Cluster 1	Abca1, Adm, Arg1, Atp7b, Bnip3, Ccl22, Cpt1b, Csf2, Cxcl3, Dgat2, Eomes, Epor, Foxp3, Gas6, Gzmm, Hif3a, Il11, Il12b, Il1a, Il1b, Il33, Irs1, Kcnn3, Lif, Lox, Mapt, P4ha2, Pim2, Sfn, Slc47a1, Ssc4d, Tlr8, Tnfrsf9, Trem1
	Cluster 2	Cps1, F2rl2, F8, Fgg, Itih3, Lamb1, Plg, Prok1, Serpina1b, Tat, Thbd
	Cluster 3	Gabrb1, Gad1

Fig. 8. Possible mechanism of piezoelectrically enhanced macrophage phagocytosis. (A) GO enrichment analysis of up-regulated DEGs between the PLGA/Zn-KNN and PLGA/Zn-KNN^{+} groups; (B) KEGG pathway enrichment analysis of up-regulated DEGs between the PLGA/Zn-KNN and PLGA/Zn-KNN^{+} groups; (C) Gene-concept network of KEGG pathway enrichment of DEGs between the control and PLGA/Zn-KNN groups; (D) Gene-concept network of KEGG pathway enrichment between the control and PLGA/Zn-KNN^{+} groups; (E) Protein-protein interaction network of DEGs between the PLGA/Zn-KNN and PLGA/Zn-KNN^{+} groups; (F) DEGs in different clusters.

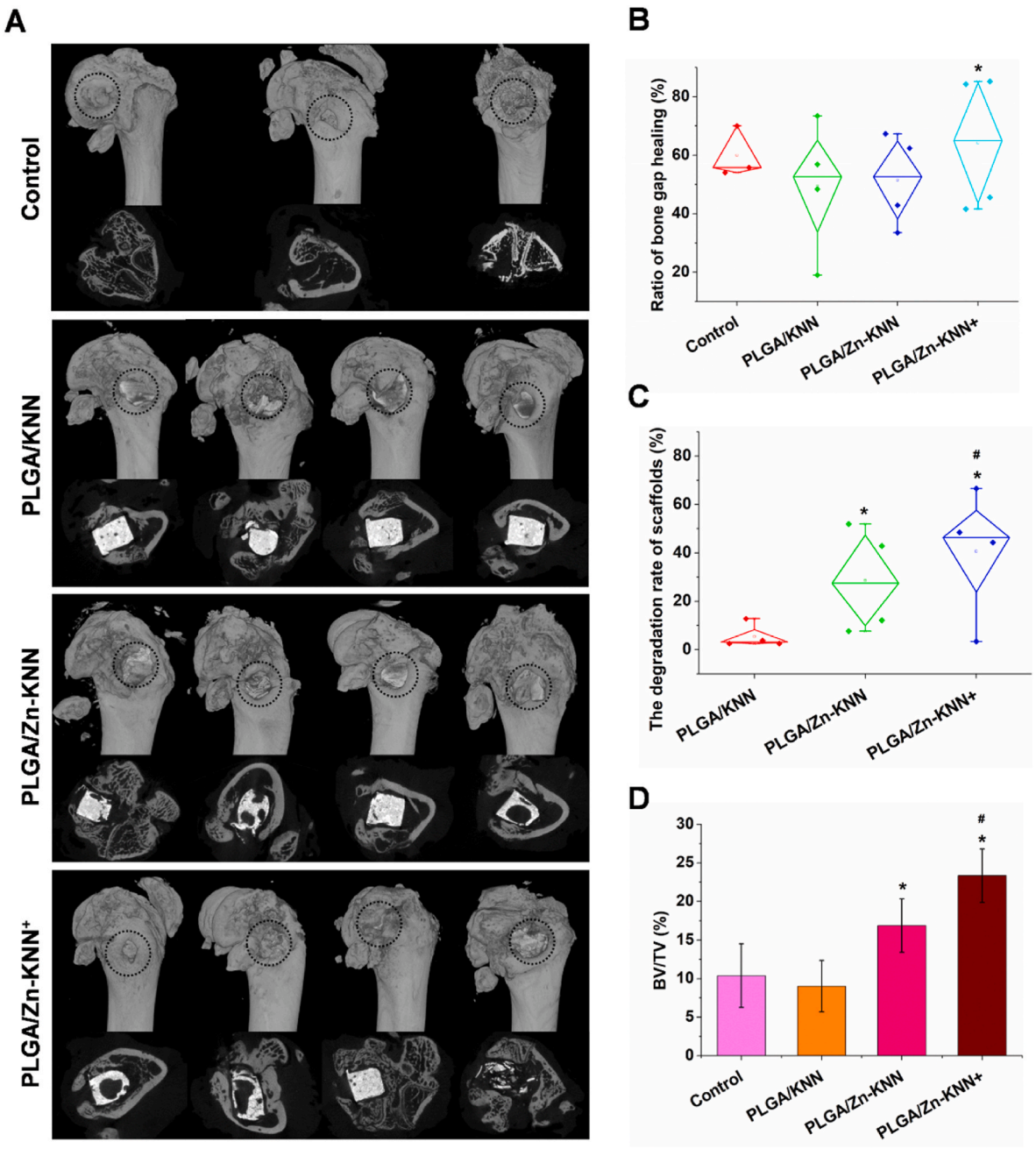

Fig. 9. In vivo anti-infection effects of piezoelectric scaffolds. (A) Reconstructed micro-CT images of femoral condylar infection in SD rats treated with various scaffolds for 2 months; (B) Quantitative analysis of the bone healing area; (C) Quantitative analysis of the degradation rate of the scaffold; (D) Quantitative analysis of the bone volume/total volume (BV/TV).

substances such as chlorine gas, hydrogen peroxide, and reactive oxygen species to kill bacteria. In addition, the pH value of the cathode is often alkaline, while the pH value of the anode is often acidic when energized, which inhibits the growth of bacteria [31]. As a common transfection method, strong electric field electroporation has been shown to disrupt bacterial cell membranes. When bacterial cells are exposed to a strong electric field, the transmembrane voltage induced by the electric field promotes the formation of pores in the lipid bilayer, causing irreversible membrane damage and even leading to bacterial death [32].

Based on the piezoelectric effect of ZnO nanoparticle array and its physical interaction with bacteria, several fabrics with high antibacterial efficiency have been removed. The piezoelectric effect of nanoparticles under bending will produce interface electrons, and the electron transfer between bacteria and nanoparticles will hinder the growth of bacteria and cause bacterial death [33]. Under ultrasonic vibration, the nanocomposites deform, which leads to the polarization potential of positive and negative charges, induces the internal piezoelectric field, and promotes the separation and migration of free electrons. The polarized composite achieved high-voltage electrocatalytic efficiency and degraded 98 % of the target organic dyes in 20 min. In addition, nanocomposites produce high concentrations of active substances, such as $\bullet O^{2-}$, and •OH radicals, which exhibit antibacterial and dye degradation capabilities [34].

There has been great interest in the regulation of immune cells by physical signals [35]. Compared with the traditional high-dose immunotherapy with side effects, a promising method to reduce the dose of immunotherapy agents for cancer patients is to combine it with electrical stimulation. Electrical stimulation can work in two ways. It can

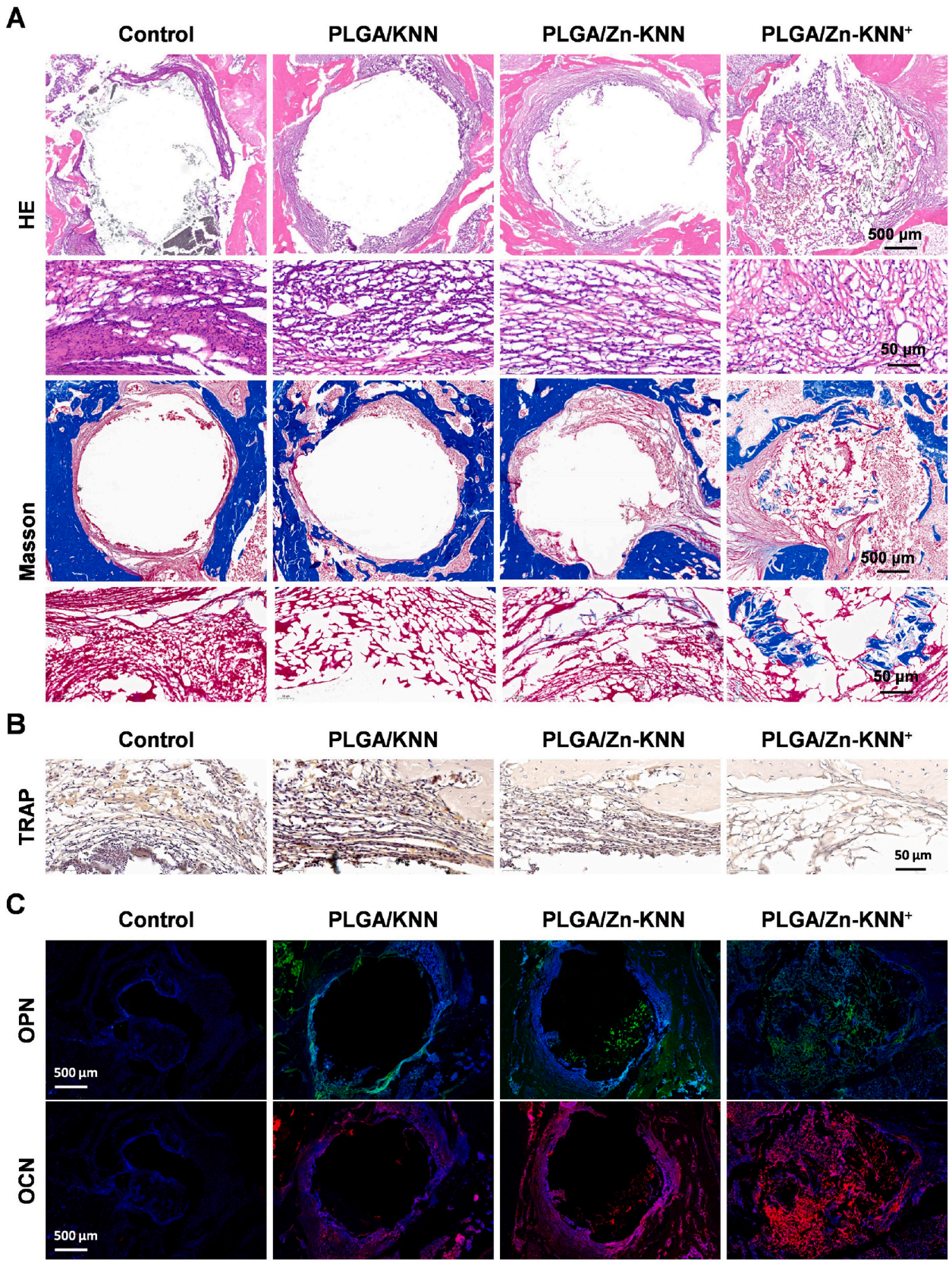

Fig. 10. In vivo histological analysis of bone infection after treatment with piezoelectric scaffolds. (A) H&E staining of histopathological bone tissue; (B) TRAP staining of histopathological bone tissue treated with various piezoelectric scaffolds and ultrasound; (C) Immunofluorescence staining of osteocalcin (OCN, red) and osteocalcin (OCN, green) proteins in different scaffold groups.

regulate the immune system, produce immune cytokines and reagents in patients, and increase the uptake of these immune reagents by cells through electroporation. Another common method is to combine electrochemical therapy with immune regulation, and improve the therapeutic effect by inducing the death of immunogenic cells or injecting immune stimulants [36]. Several therapies use electroporation to deliver immunostimulants more effectively (e.g., genes encoded by sequences that produce cytokines, cancer specific antigens, or anti-tumor toxin fragments). As an important type of physical stimulation, electrical signals have attracted more and more attention in the biomedical field, and can directly program cell behavior in the way of electro genetics. However, few studies have focused on how electrical signals regulate macrophage polarization. Under physiological or pathological conditions, cell death and tissue damage will lead to ion current fluctuations in the cell microenvironment, which will also affect the potential of the microenvironment. Therefore, electrical stimulation may have an important effect on macrophage polarization by regulating the cell microenvironment. Recent studies shows that PVDF piezoelectric materials have been used to mediate non-invasive local electrical signals through ultrasonic stimulation to enhance the inflammatory response of macrophages [37]. This strategy relies on the tiny vibration and local charge release of β-PVDF film under ultrasonic conditions, which significantly triggers the selective expression and secretion of pro-inflammatory factors. In the process, voltage-gated channels promoted Ca^{2+} influx and stimulated M1 polarization of macrophages through the Ca^{2+}-CAMK2A-NF-κB signaling pathway. M1 macrophages secrete inflammatory factors, which significantly inhibit the activity of tumor cells co-cultured with M1 macrophages. The study shows that the electrical signal mediated by piezoelectric materials can regulate the immune process and provide a controllable non-invasive electrical stimulation to drive the inflammatory response, which is of great significance for tumor immunotherapy.

In the current study, the main function of the PLGA/Zn-KNN^{+} is to upregulate complement and coagulation cascades, which can cooperate with other immune molecules to attack and remove pathogens such as bacteria, viruses, fungi, etc., and directly kill some bacteria by bacteriolysis, which are ingested and digested by macrophages under phagocytosis [38]. At the same time, some signaling pathways that promote the phenotype of M1 macrophages, such as Chemokine signaling pathway, Cytokine-cytokine receptor interaction, IL-17 signaling pathway, JAK-STAT signaling pathway, TNF signaling pathway, are activated [39]. According to the PPI network results, the Lmab1 may play a vital role in regulating macrophage immunological functioning. Cells have passive reactivity towards the biochemical and biophysical signals (such as electrical signals) transmitted by the extracellular matrix, which can effectively regulate various biological processes and serve as an external intervention to promote the synthesis of extracellular matrix [40]. Another study found that adhesion to different extracellular matrix ligands had only moderate effects on the secretion of cytokines stimulated by prototype activation by macrophages. However, compared with collagen, fibronectin or fibrinogen, the expression of arginase-1, a marker of healing promoting phenotype, was enhanced when cells were cultured on laminin, matrix glue and vitronectin. When micropattern into lines, almost all matrix ligands allow macrophages to elongate, accompanied by an increase in arginase-1 expression. Together, these data suggest that extracellular matrix composition and adhesion geometry affect the shape and function of macrophages [41]. Although many people know how soluble factors, including cytokines and chemokines, affect the function of immune cells [42], little is known about how insoluble cues (including those provided by the matrix) regulate their behavior. Further research is needed to understand the potential role of different adhesion proteins and their geometric expression in regulating macrophage behavior.

Based on these findings, we proposed a model depicting the molecular mechanisms by which the PLGA/Zn-KNN piezoelectric scaffold treats bone infection by regulating macrophage M1 polarization and enhancing phagocytosis (Fig. 11). PLGA/Zn-KNN^{+} may activate Laminin-integrin signaling pathway mediated complement and coagulation cascades, and then indirectly activated M1 macrophage phenotype-related signaling pathway, which digested and ingested bacteria under phagocytosis. Therefore, the immunomodulation therapy based on antibacterial piezoelectric materials is convenient and avoid the selective pressure caused by the evolution of bacterial drug resistance to the greatest extent. In addition, this non-specific immune defense can be used to prevent many pathogenic bacteria, especially in high-risk population, and to identify and treat early infectious diseases.

4. Conclusion

In this work, a biodegradable PLGA/Zn-KNN piezoelectric scaffold has been developed, which simultaneously served as both a biodegradable antibacterial tissue scaffold and a controllable electrical stimulator. The incorporation of ZnO into KNN greatly enhances the piezoelectric performance of Zn-KNN particles, exhibiting inherently solubility and degradation behavior. The PLGA/Zn-KNN piezoelectric scaffold released zinc ions, and electrical stimulation driven by ultrasound resulted in significant antibacterial effects through direct and immunoregulatory antibacterial pathways. Mechanistic investigation suggested that extracellular matrix ligands and complement and coagulation cascade may have moderate effects on macrophage phagocytosis. These findings are of great significance for understanding the application of electrostimulation materials in medical technology and provide guidance for immunoantimicrobial therapy in clinical infections.

5. Materials and methods

Synthesis of the KNN and Zn-KNN Particles: The KNN particles were synthesized via a solid-state reaction. Briefly, KCl, K_2CO_3, and Nb_2O_5 were mixed in 11: 1: 4 ratios by ball milling and then calcined at 1000 °C for 3 h in a high temperature resistant crucible. The synthesized of KNN particle precursors were soaked in a 2 M of nitric acid solution and washed with deionized water and dried in the blast drying oven. Ulteriorly, the above KNN particle precursors were completely transformed into KNN particles through calcined in a crucible at 850 °C for 10 min after mixed with Na_2CO_3, NaCl, KCl, and K_2CO_3 in 3: 11: 1:11 ratios by ball milling. Finally, the KNN particles were collected by washing and drying in the blast drying oven. For the Zn-KNN composite preparation, the prepared KNN particles and ZnO nanoparticles (30 nm, Aladdin) were mixed in 20: 1 ratio by ball milling in alcohol for 24 h. After drying, the samples were sintered in a covered alumina crucible at 850 °C for 15 min.

Fabrication of PLGA/KNN and PLGA/Zn-KNN Scaffolds: 1 g of KNN or Zn-KNN particles was dispersed in 1 mM of Tris-HCl aqueous solution (pH 8.6), followed by ultrasonic treatment (50 kHz) for 60 min and stirring evenly for 2 h. Then, 0.1 g of dopamine hydrochloride (DA-HCl) was transferred to the above mixed solution and stirred for 12 h. Finally, the mixed solution was washed and dried in a vacuum oven to obtain polydopamine (PDA) modified particles. Then, 0.5 g of PDA modified KNN or Zn-KNN particles was dispersed into 10 mL of hexafluoro isopropanol by ultrasound (50 kHz) for 60 min and stirring for 2 h, and 1 g of PLGA powders were added to the above solution and stirred for 2 h to form a homogeneous solution. Subsequently, the PLA/KNN and PLA/Zn-KNN scaffolds were prepared using polytetrafluoroethylene molds.

Characterization of the Particles and Scaffolds: A scanning electron microscopy (SEM, Nova Nano SEM 450) was used to characterize the morphology and microstructure of KNN and Zn-KNN particles and scaffolds. The K, Na, Nb and Zn distributions in KNN and Zn-KNN particles and scaffolds were scanned with an energy dispersive spectrometer (EDS, Ultim-Max 40). An X-ray diffractometer (XRD, Smart Lab-SE) was employed to determine the crystalline phases of the particles using Cu Kα radiation ($\lambda = 1.5418$ Å) at a scanning rate of 4° min^{-1}. A high-

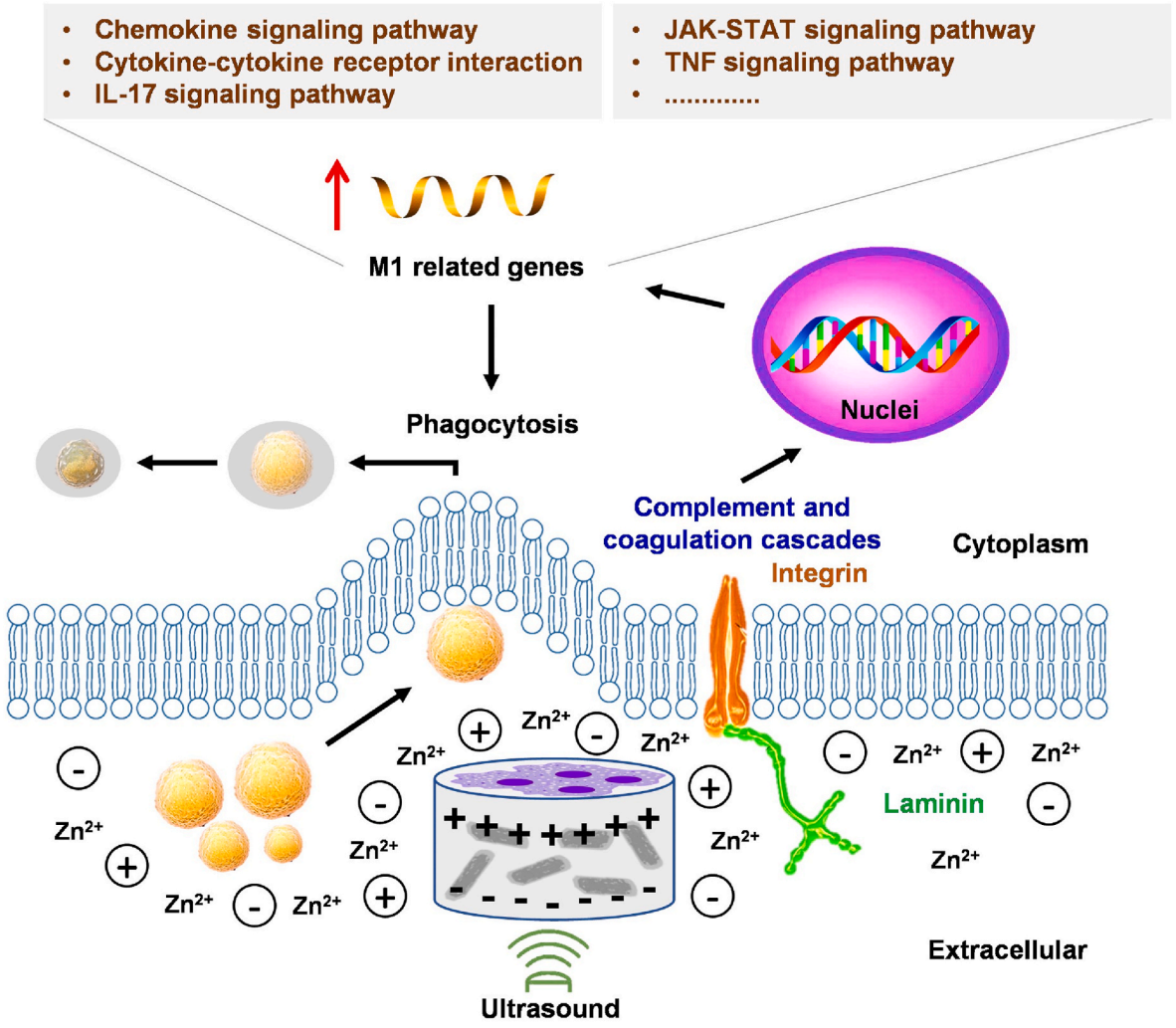

Fig. 11. Schematic diagram of the possible molecular mechanism by which the PLGA/Zn-KNN piezoelectric scaffold treats bone infection by regulating macrophage M1 polarization and enhancing phagocytosis.

resolution transmission electron microscopy (HRTEM, JEM-2100F) observation was carried out using an electron microscope. The functional group changes in the scaffolds were tested by Fourier transform infrared spectroscopy (FTIR, TNZ1-5700). A digital storage oscilloscope (RTM3000) and a current amplifier (CX3300) were used to record the changes in the output voltage of the scaffolds after they were subjected to external periodic high-frequency ultrasound (frequency:100 kHz, pulse period: 0.5 s).

Ion Release of Scaffolds: The PLGA/KNN and PLGA/Zn-KNN scaffolds were immersed in 9 mg/L of NaCl solution. The mixed solution was centrifuged (10000 rpm) for 5 min to collect the supernatant, which was reimmersed with fresh 9 mg/L of NaCl solution for dilution at 37 °C. The supernatant samples were collected every 3 days for 2 weeks. Then, an inductively coupled plasma-optical emission spectrometer (ICP-AES, Optima 4300DV) was used to measure the concentrations of Zn^{2+} and Nb^{5+} in the supernatant.

Vienna Ab Initio Simulation: The piezoelectric performances of zinc oxide/potassium solid niobate vacuum heterojunctions and potassium solid niobate were compared by using the Vienna Ab initio Simulation Package (VASP). To accurately obtain and compare the piezoelectric properties of the PLGA/KNN and PLGA/Zn-KNN scaffolds, it is necessary to calculate their piezoelectric constant d_{ij} and piezoelectric tensor e_{ij}, and pay attention to the elastic constant c_{ij}. First, VASP was used to optimize the geometric structure of the zinc oxide/potassium solid niobate vacuum heterojunction and potassium solid niobate to ensure accurate calculations. During the optimization process, adjustments to the lattice parameters and atomic positions should be considered until the energy and force converge. The stress-strain relationship was calculated to obtain the elastic constant matrix of the material. By utilizing the built-in functionality of VASP, the piezoelectric tensor was obtained by applying small strains and calculating the system's polarization. By combining the elastic constant and piezoelectric tensor, the piezoelectric constant can be obtained through the following relationship:

$$d_{ij} = e_{ij} \bullet s_{ij}$$

Among them, s_{ij} is the elastic compliance matrix (i.e., the inverse matrix of c_{ij}). The piezoelectric properties of zinc oxide/potassium solid niobate vacuum heterojunctions and potassium solid niobate were comprehensively compared to clarify their advantages and differences in practical applications.

Cell viability analyses: Rat BMSCs were harvested from male Wistar rats. The cells were dispersed, centrifuged (1000 rpm, 10 min) and resuspended in α-MEM with 20 % FBS, seeded into 25 cm^2 plastic flasks, and incubated at 37 °C humidified atmospheres with 5 % CO_2 for 24 h before the first medium was changed. Then, the medium was replaced every 3 days and the cells were used after 1 week. Passage 2–5 BMSCs were used in all experiments. The cultured BMSCs were then seeded at 100000 cells/cm^2 in α-MEM supplemented containing 10 % fetal bovine serum, 1 % penicillin and streptomycin, and the medium was renewed

every 3 days. The cell proliferation assay was performed to evaluate the viability and survival of bone marrow mesenchymal stem cells (BMSCs) on PLGA/KNN scaffold, PLGA/Zn-KNN scaffold, and PLGA/Zn-KNN scaffold with ultrasound exposure. In detail, the BMSCs, were inoculated on the sterilized scaffolds in 96 well plates, respectively. And the cultural medium was employed as the control group. After culture for 1, 3 and 5 days, the cell viability was investigated using the CCK-8 assay as the per kit directions to evaluate the effect of ultrasound and PLGA/Zn-KNN scaffolds on the proliferation of cells. BMSCs treated for 3 days with PLGA/KNN and PLGA/Zn-KNN scaffolds and ultrasound (+) were stained with TRITC phalloidin (5 μg/mL) and DAPI (5 μg/mL) to show the cytoskeleton and cellular nuclei respectively. The BMSCs cell status at day 1 was assessed by using the live-dead cell staining with Calcein-acetoxymethyl ester (Calcein-AM)/propidium iodide (PI) double staining. The cells were observed by a fluorescence microscope (Olympus IX71, Japan).

Osteogenesis in vitro: To assess the osteogenic differentiation capacity of BMSCs under the treatment of PLGA/KNN scaffold, PLGA/Zn-KNN scaffold, and PLGA/Zn-KNN scaffold with ultrasound exposure, 2 $\times 10^5$ cells and various scaffolds were seeded into the 24-well plates and cultured with the BMSCs cell medium supplemented with 10 mm β-glycerolphosphate, 10 nm dexamethasone and vitamin D. On day 7, the cells were fixed by the 4 % paraformaldehyde, stained with a BCIP/NBT ALP color development kit and captured by the stereo microscope. On day 14, the samples were isolated with Trizol reagent (Invitrogen, USA) for the total RNA. And the RNA was transcribed into complementary DNA (cDNA) with the cDNA Synthesis kit (Sigma Aldrich). The specific primers were listed in Table S3, and the mRNA relative expression was expressed using the $2^{-\Delta\Delta CT}$ method.

Ultrasound Treatment of Bacterial Strains with Scaffolds: For the ultrasound treatment experiments, *Escherichia coli* (*E. coli)* and *Methicillin-resistant Staphylococcus aureus (MRSA)* were grown overnight under 180 rpm of shaking at 37 °C in LB media supplemented with 10 g/L of peptone, 7 g/L of beef exact, and 5 g/L of NaCl. Subsequently, the *E. coli and MRSA* were washed in PBS and centrifuged for 5 min, and then diluted with PBS to a density of 1∼5 $\times 10^7$ CFU/mL based on the optical density value. 200 μL of *E. coli and MRSA* suspension was mixed with ZnO (0.14 mg/mL, equal to the zinc oxide content in 9 mg PLGA/Zn-KNN), PLGA/KNN (9 mg/mL) and PLGA/Zn-KNN (9 mg/mL) scaffolds, and then diluted with PBS to a final volume of 4 mL in a sterile microcentrifuge tube. The groups included the control, PLGA/KNN scaffold, PLGA/Zn-KNN scaffold, and PLGA/Zn-KNN scaffold with ultrasound exposure (frequency:100 kHz, pulse period: 0.5 s) at 37 °C for 25 min. After ultrasound treatment, the number of surviving bacteria was determined by the colony counting method. Simply put, each sample was continuously diluted with PBS to a final volume of 10^7-fold. Then, 200 μL of diluted *E. coli and MRSA* suspension was applied to the surface of LB agar plates. After incubated at 37 °C for 24 h, the number of viable *E. coli and MRSA* bacterial colonies was counted in CFU/mL. The number of viable bacterial was determined by measuring the absorbance at 600 nm using a microplate reader.

Bacterial Live/Dead Staining Assay: An AO/EB staining kit was used to qualitatively determine the integrity of *E. coli and MRSA* bacterial cell membranes. 5–8 $\times 10^7$ CFU/mL of fresh *E. coli and MRSA* bacterial suspension in PBS was mixed with PLGA/KNN (9 mg/mL) and PLGA/Zn KNN scaffolds (9 mg/mL), and then diluted with PBS in a sterile micro centrifuge tube to the final volume of 4 mL. The mixture in different micro centrifuge tubes was then exposed to ultrasound (frequency:100 kHz, pulse period: 0.5 s) at 37 °C for 25 min. The control group without exposure to ultrasound was incubated at 37 °C for 25 min. After different treatments, 1 μM AO and 2 μM EB were added, and the mixture was incubated in the dark for 10 min. Then, the excess AO and EB dyes were washed with PBS. Finally, *E. coli and MRSA* bacterial were observed with a fluorescence microscope (Olympus IX71) at the excitation wavelength of 488 nm.

Morphological Macrophage Phagocytosis Assay: Mouse mononuclear macrophage cells (RAW264.7) were purchased from China Center for Type Culture Collection (Shanghai, China). The complete medium for RAW264.7 cells included 500 mL of high glucose medium (Gibco), 10 mL of fetal bovine serum (Gibco), and 5 mL of penicillin/streptomycin solution (Gibco). During cell culture, the medium was changed every 2 days. The complete medium used for RAW264.7 cells included 500 mL of high glucose medium (Gibco), 10 mL of fetal bovine serum (Gibco), and 5 mL of penicillin/streptomycin solution (Gibco). The medium was changed every 2 days during cell culture. A confluent RAW264.7 cells were cocultured on PLGA/KNN and PLGA/Zn-KNN scaffolds with or without ultrasound treatment for 2 days. Then, CFDA-labeled *E. coli and MRSA* were added to the wells and co-cultured with RAW264.7 cells for 1 h. Finally, the phagocytosis results were observed and recorded using a fluorescence microscope. For TEM, the medium was replaced with gradient acetone after dehydration, and the cells were impregnated with an embedding agent overnight. After crosslinking polymerization at 37 °C, 45 °C, and 60 °C for 12 h, the samples were cut into thin slices with a thickness of about 80 nm using an ultrath in microtome (Leica emuc7). For visualization, uranyl acetate and lead dye solutions were used for double staining. Finally, TEM images were taken on HITACHI H-7000FA at accelerating voltage. For visualization at 2500 × and 10000 × magnification.

Immunofluorescence Staining: RAW264.7 cells were cultured on piezoelectric scaffolds for 2 days, then fixed with 4 % paraformaldehyde for 30 min at 37 °C. The fixed RAW264.7 cells were permeabilized for 5 min at 25 °C by using 0.1 % of Triton-X-100 and blocked for 30 min at 25 °C by using 1 % of BSA/PBS. The fixed RAW264.7 cells were washed with PBS and incubated with primary TNF-α (1:800; 60291-1-lg; Proteintech) and CD86 (1:800; 13395-1-AP; Proteintech) antibodies at 4 °C for 24 h. After washed with PBS 3 times, the fixed RAW264.7 cells were added with the Cy3-conjugated Affinipure Goat Anti-Rabbit IgG(H + L) secondary antibody (SA00009-2; Proteintech) and fluorescein (FITC)-conjugated Affinipure Goat Anti-Rabbit IgG(H + L) secondary antibody (SA00003-2; Proteintech) in 1 % BSA/PBS and incubated at 4 °C for 24 h. After washed with PBS 3 times, the fixed RAW264.7 cells were then stained with 4′, 6-Diamidine-2-phenylindole (DAPI) and recorded by using a laser scanning confocal microscope (Olympus FV4000, Japan).

RNA Sequencing: RNA seq technology was used to detect the gene expression profiles of macrophages cultured on PLGA/KNN and PLGA/Zn-KNN scaffolds after 2 days of ultrasound treatment. Then, following the manufacturer's instructions, total RNA from macrophages was collected in each group using TRIzol reagent (Invitrogen). RNA sequencing was performed by Bioyi Biotechnology (Wuhan, China). Use heatmap (v1.0.8) to draw heatmaps of gene expression levels in different samples. In short, differential expression analysis was performed using DESeq2 (v1.4.5) with a Q value ≤ 0.05. In order to gain a deeper understanding of phenotypic changes, Phyper was used to perform Gene Ontology (GO) and Kyoto Encyclopedia of Genes and Genomes (KEGG) enrichment analysis on differentially expressed genes based on hypergeometric tests. According to a strict Q-value threshold (Q-value $\leq$0.05), Bonferroni correction was used to adjust the significance levels of terms and pathways.

Rat Femoral Condylar Infection Model: The experimental rats were purchased from the Jiling Provincial Center for Disease Control and Prevention (Jiling, China). All animal experiments were carried out according to the protocol approved by the Institutional Animal Care and Use Committee of Jiling University (2021279). To establish the *MRSA* infected femur defect model, a defect of 250 g in male SD rats with a φ3 × 3 mm was made on the femoral condyle and the mixed bacterial solution (1 $\times 10^8$ CFU/mL, 10 μL) was slowly injected into the defect cavity. Then, the scaffolds from the following four groups were implanted. The groups included control, PLGA/KNN scaffold, PLGA/Zn-KNN scaffold, and PLGA/Zn-KNN scaffold with ultrasound exposure (n = 4). Rats on the PLGA/Zn-KNN scaffold were exposed to ultrasound (frequency:100 kHz, pulse period: 0.5 s) for 60 min every other day for 4 weeks after the operation.

Micro-computed Tomography: The rats were killed 8 weeks after the operation and fixed for 24 h. Then, the skull samples were scanned by a SkyScan 1176 micro-computed tomography (micro-CT, Bruker) using a monochromatic beam with 30 keV energy and a resolution ratio of 18 μm, and CTVox software and CTAn software were used to process the images and data by extracting voxels with a gray value of 130. The bone healing area, degradation rate of the scaffold, and bone tissue volume/total tissue volume (BV/TV) were analyzed based on the reconstructed micro-CT images.

Histological Analysis: The rats were sacrificed 8 weeks after the operation. The skull samples were cut into 7 μm thick sections, and then stained with histopathological Hematoxylin and Eosin (H&E), Masson's trichrome and Gram staining. For immunohistochemistry and immunofluorescence staining, slices were defatted with paraffin, covered with antigen recovery solution at 95–100 °C, and blocked with 5 % goat serum for 30 min. Primary osteopontin (OPN) polyclonal antibody (1:50, 22952-1-AP, Proteintech), osteocalcin (OCN) polyclonal antibody (1:200, 23418-1-AP, Proteintech), tartrate resistant acid phosphatase (TRAP) polyclonal antibody (1:50, 11594-1-AP, Proteintech) were used. A secondary antibody (1:200, Vector laboratories) and DAB substrate kit (Vector laboratories) were used for immunohistochemistry staining. A secondary antibody cy3-conjugated Affinipure goat anti-rabbit IgG (H + L) and fluorescein (FITC)-conjugated Affinipure goat anti-rabbit IgG (H + L) were used for immunofluorescence staining. The sections were imaged by using a pathological section scanner (MDS-MLF05, Hangzhou Medipath).

Statistical Analysis: Statistical analysis was performed with SPSS 18 software (IBM SPSS, USA). The data were expressed as the mean ± standard deviation (SD). For multiple group comparisons, one-way analysis of variance (ANOVA) was used. For a single comparison between two groups, paired Student's t-tests were used. The significance level was set at $P < 0.05$.

CRediT authorship contribution statement

Yuhao Zheng: Writing – original draft. **Shu Wang:** Investigation. **Wenhe Jin:** Methodology. **Zhuoxuan Li:** Data curation, Writing – review & editing. **Guoju Yang:** Methodology. **Xiaoxu Li:** Formal analysis. **Ning Li:** Data curation. **Yue Wang:** Validation. **Fan Sheng:** Data curation. **Zhiming Song:** Writing – review & editing.

Data availability statement

The data that support the findings of this study are available from the corresponding author upon reasonable request.

Ethics approval and consent to participate

All animal experiments were carried out according to the protocol approved by the Institutional Animal Care and Use Committee of Jiling University (2021279).

Declaration of competing interest

The authors declare that they have no known competing financial interests or personal relationships that could have appeared to influence the work reported in this paper.

Acknowledgements

This work was supported by grants from the Key R&D Projects of the Science and Technology Development Plan of Jilin Province, China (20220204126YY), the Medical and Health Talent Special Project of Jilin Province, China (JLSWSRCZX2023-32), and the Natural Science Foundation Discipline Layout Project of Jilin Province, China (20200201478JC).

Appendix A. Supplementary data

Supplementary data to this article can be found online at https://doi.org/10.1016/j.bioactmat.2025.01.026.

References

[1] B. Jia, X. Du, W. Wang, et al., Nanophysical antimicrobial strategies: a rational deployment of nanomaterials and physical stimulations in combating bacterial infections, Adv. Sci. 9 (10) (2022) e2105252, https://doi.org/10.1002/advs.202105252.

[2] F. Liu, X. Wang, T. Chen, et al., Hydroxyapatite/silver electrospun fibers for anti-infection and osteoinduction, J. Adv. Res. 21 (2019) 91–102, https://doi.org/10.1016/j.jare.2019.10.002.

[3] A. El-Fiqi, N. Mandakhbayar, S.B. Jo, J.C. Knowles, J.H. Lee, H.W. Kim, Nanotherapeutics for regeneration of degenerated tissue infected by bacteria through the multiple delivery of bioactive ions and growth factor with antibacterial/angiogenic and osteogenic/odontogenic capacity, Bioact. Mater. 6 (1) (2020) 123–136, https://doi.org/10.1016/j.bioactmat.2020.07.010.

[4] F. Frost, M. Shaw, D. Nazareth, Antibiotic therapy for chronic infection with *Burkholderia cepacia* complex in people with cystic fibrosis, Cochrane Database Syst. Rev. 12 (12) (2021) CD013079, https://doi.org/10.1002/14651858.CD013079.pub3.

[5] S.J. Cole, C.L. Hall, M. Schniederberend, et al., Host suppression of quorum sensing during catheter-associated urinary tract infections, Nat. Commun. 9 (1) (2018) 4436, https://doi.org/10.1038/s41467-018-06882-y.

[6] Youwen Yang, Chenrong Ling, Yageng Li, Shuping Peng, Deqiao Xie, Lida Shen, Zongjun Tian, Cijun Shuai, Microstructure development and biodegradation behavior of additively manufactured Mg-Zn-Gd alloy with LPSO structure, J. Mater. Sci. Technol. 144 (2023) 1–14, https://doi.org/10.1016/j.jmst.2022.09.059.

[7] L. Chenrong, L. Qiang, Z. Zhe, Y. Youwen, Z. Wenhao, C. Wenlong, D. Zhi, P. Chunrong, S. Cijun, et al., Influence of heat treatment on microstructure, mechanical and corrosion behavior of WE43 alloy fabricated by laser-beam powder bed fusion, Int. J. Extrem. Manuf. 6 (1) (2024), https://doi.org/10.1088/2631-7990/acfad5.

[8] Y. Cai, W. Bing, X. Xu, Y. Zhang, Z. Chen, Z. Gu, Topographical nanostructures for physical sterilization, Drug Deliv Transl Res 11 (4) (2021) 1376–1389, https://doi.org/10.1007/s13346-021-00906-9.

[9] S. Tian, H. Bai, S. Li, et al., Water-soluble organic nanoparticles with programable intermolecular charge transfer for NIR-II photothermal anti-bacterial therapy, Angew Chem. Int. Ed. Engl. 60 (21) (2021) 11758–11762, https://doi.org/10.1002/anie.202101406.

[10] Y. Zhao, L. Hu, H. Dai, P. Zhuang, K. Huang, W. Hou, J. Liu, R. Tu, T. Goto, Smart trap-capture-kill antibacterial system for infected microenvironment improvement and vascularized bone regeneration via magnetic thermotherapy, Adv. Funct. Mater. 33 (23) (2023) 2214734, https://doi.org/10.1002/adfm.202214734.

[11] Y. Wei, Y. Zhang, W. Geng, H. Su, M. Long, Efficient bifunctional piezocatalysis of Au/BiVO4 for simultaneous removal of 4-chlorophenol and Cr (VI) in water, Appl. Catal. B Environ. 259 (2019) 118084, https://doi.org/10.1016/j.apcatb.2019.118084, 15.

[12] X. Chen, L. Liu, Y. Feng, L. Wang, Z. Bian, H. Li, Z.L. Wang, Fluid eddy induced piezo-promoted photodegradation of organic dye pollutants in wastewater on ZnO nanorod arrays/3D Ni foam, Mater. Today 20 (9) (2017) 501–506, https://doi.org/10.1016/j.mattod.2017.08.027, 1.

[13] E. Sun, W. Cao, Relaxor-based ferroelectric single crystals: growth, domain engineering, characterization and applications, Prog. Mater. Sci. 65 (2014) 124–210, https://doi.org/10.1016/j.pmatsci.2014.03.006.

[14] Z. Zhu, X. Gou, L. Liu, et al., Dynamically evolving piezoelectric nanocomposites for antibacterial and repair-promoting applications in infected wound healing, Acta Biomater. 157 (2023) 566–577, https://doi.org/10.1016/j.actbio.2022.11.061.

[15] J. Zhang, Q. Bai, X. Bi, et al., Piezoelectric enhanced peroxidase-like activity of metal-free sulfur doped graphdiyne nanosheets for efficient water pollutant degradation and bacterial disinfection, Nano Today (43) (2022) 43, https://doi.org/10.1016/j.nantod.2022.101429.

[16] P. Chen, C. Xu, P. Wu, et al., Wirelessly powered electrical-stimulation based on biodegradable 3D piezoelectric scaffolds promotes the spinal cord injury repair, ACS Nano 16 (10) (2022) 16513–16528, https://doi.org/10.1021/acsnano.2c05818.

[17] C. Liu, X. Xie, W. Zhao, et al., Conducting nanosponge electroporation for affordable and high-efficiency disinfection of bacteria and viruses in water, Nano Lett. 13 (9) (2013) 4288–4293, https://doi.org/10.1021/nl402053z.

[18] Li-Qian Cheng, Ke Wang, Jingfeng Li, Synthesis of complex niobate nanostructures via molten-salt reaction: effect of ZrO2 on product morphology, Mater. Lett. 138 (2015) 128–131, https://doi.org/10.1016/J.MATLET.2014.09.096.

[19] M. Godoy-Gallardo, U. Eckhard, L.M. Delgado, et al., Antibacterial approaches in tissue engineering using metal ions and nanoparticles: from mechanisms to applications, Bioact. Mater. 6 (12) (2021) 4470–4490, https://doi.org/10.1016/j.bioactmat.2021.04.033.

[20] Y. Wang, J. Liu, T. Wang, et al., Antibacterial properties and mechanism of nanometer zinc oxide composites, Food Packag. Shelf Life 40 (2023), https://doi.org/10.1016/j.fpsl.2023.101167.

[21] L. Yilong, W. Chuilei, Z. Yuanna, H. Limin, W. Tao, W. Tongzhen, H. Yu, et al., Role of ZnO dopant in enhancing piezoelectric characteristics in KNN-based piezoelectric ceramics, J. Am. Ceram. Soc. (2024), https://doi.org/10.1111/jace.20186.
[22] N. Yang, Y. Liu, The role of the immune microenvironment in bone regeneration, Int. J. Med. Sci. 18 (16) (2021) 3697–3707, https://doi.org/10.7150/ijms.61080.
[23] Yueming Li, Jinsong Wang, Runhua Liao, Dan Dan Huang, Xiangping Jiang, Synthesis and piezoelectric properties of KxNa1−xNbO3 ceramic by molten salt method, J. Alloys Compd. 496 (2010) 282–286, https://doi.org/10.1016/J.JALLCOM.2010.01.139.
[24] B. Mi, L. Chen, Y. Xiong, et al., Osteoblast/osteoclast and immune cocktail therapy of an exosome/drug delivery multifunctional hydrogel accelerates fracture repair, ACS Nano 16 (1) (2022) 771–782, https://doi.org/10.1021/acsnano.1c08284.
[25] S. Cijun, Z. Jun, D. Fang, Y. Youwen, P. Shuping, Z. Zhenyu, et al., Core–shell-Structured ZIF-8@PDA-HA with controllable zinc ion release and superior bioactivity for improving a poly-l-lactic acid scaffold, ACS Sustain. Chem. Eng. 9 (4) (2021) 1814–1825. Doi:org/10.1021/.
[26] Y. Xiong, Z. Lin, P. Bu, et al., A whole-course-repair system based on neurogenesis-angiogenesis crosstalk and macrophage reprogramming promotes diabetic wound healing, Adv. Mater. 35 (19) (2023 May) e2212300, https://doi.org/10.1002/adma.202212300. PMID: 36811203.
[27] Z. Pan, J. Chen, L. Fan, J. Zhang, S. Zhang, Y. Huang, L. Liu, L. Fang, X. ng, Enhanced piezoelectric properties and thermal stability in the (K0. 5Na0. 5) NbO3: ZnO lead-free piezoelectric composites, J. Am. Ceram. Soc. 98 (12) (2015 Dec) 3935–3941.
[28] H.S. Devi, M. Maisnam, Effect of ZnO additions to Na0. 47K0. 47Li0. 06NbO3 ceramics prepared by ceramic method using high energy ball milling and sintered by microwave technique. InIOP Conference Series: Materials Science and Engineering vol. 577, IOP Publishing, 2019 Nov 1 012150, https://doi.org/10.1088/1757-899X/577/1/012150, 1.
[29] H. Cho, A. Naskar, S. Lee, S. Kim, K.S. Kim, A new surface charge neutralizing nano-adjuvant to potentiate polymyxins in killing mcr-1 mediated drug-resistant Escherichia coli, Pharmaceutics 13 (2) (2021) 250, https://doi.org/10.3390/pharmaceutics13020250. Published 2021; 11.
[30] B.A. Costa, M.P. Abuçafy, T.W.L. Barbosa, et al., ZnO@ZIF-8 nanoparticles as nanocarrier of ciprofloxacin for antimicrobial activity, Pharmaceutics 15 (1) (2023) 259, https://doi.org/10.3390/pharmaceutics15010259. Published 2023; 11. dpi:.
[31] Jiwei Li, Yu Jun Feng, Weichao Chen, Shaohua Zhang, Jianwei Ma, Shaojuan Chen, Shangpeng Liu, Chengbo Cao, Yuankai Zhang, Electroactive materials: innovative antibacterial platforms for biomedical applications, Prog. Mater. Sci. 132 (2022) 101045, https://doi.org/10.1016/j.pmatsci.2022.101045.
[32] J. Li, Y. Feng, W. Chen, S. Zhang, J. Ma, S. Chen, S. Liu, C. Cao, Y. Zhang, Electroactive materials: innovative antibacterial platforms for biomedical applications, Prog. Mater. Sci. 132 (2023) 101045, https://doi.org/10.1016/j.pmatsci.2022.101045, 1.
[33] T. Wang, H. Chen, C. Yu, X. Xie, Rapid determination of the electroporation threshold for bacteria inactivation using a lab-on-a-chip platform, Environ. Int. 132 (2019) 105040, https://doi.org/10.1016/j.envint.2019.105040.
[34] Y. Wang, K.K. Liu, W.B. Zhao, J.L. Sun, X.X. Chen, L.L. Zhang, Q. Cao, R. Zhou, L. Dong, C.X. Shan, Antibacterial fabrics based on synergy of piezoelectric effect and physical interaction, Nano Today 48 (2023) 101737, https://doi.org/10.1016/j.nantod.2022.101737, 1.
[35] W. Ma, M. Lv, F. Cao, Z. Fang, Y. Feng, G. Zhang, Y. Yang, H. Liu, Synthesis and characterization of ZnO-GO composites with their piezoelectric catalytic and antibacterial properties, J. Environ. Chem. Eng. 10 (3) (2022) 107840, https://doi.org/10.1016/j.jece.2022.107840, 1.
[36] M. Uemura, N. Maeshige, A. Yamaguchi, et al., Electrical stimulation facilitates NADPH production in pentose phosphate pathway and exerts an anti-inflammatory effect in macrophages, Sci. Rep. 13 (1) (2023) 17819, https://doi.org/10.1038/s41598-023-44886-x.
[37] R. Das, S. Langou, T.T. Le, P. Prasad, F. Lin, T.D. Nguyen, Electrical stimulation for immune modulation in cancer treatments, Front. Bioeng. Biotechnol. 9 (2022) 795300, https://doi.org/10.3389/fbioe.2021.795300.
[38] Y. Kong, F. Liu, B. Ma, et al., Wireless localized electrical stimulation generated by an ultrasound-driven piezoelectric discharge regulates proinflammatory macrophage polarization, Adv. Sci. 8 (13) (2021) 2100962, https://doi.org/10.1002/advs.202100962.
[39] E.M. Conway, Complement-coagulation connections, Blood Coagul. Fibrinolysis 29 (3) (2018) 243–251, https://doi.org/10.1097/MBC.0000000000000720.
[40] X. Hu, J. Chen, L. Wang, L.B. Ivashkiv, Crosstalk among Jak-STAT, Toll-like receptor, and ITAM-dependent pathways in macrophage activation, J. Leukoc. Biol. 82 (2) (2007) 237–243, https://doi.org/10.1189/jlb.1206763.
[41] Li Chen, Jianye Yang, Zhengwei Cai, Yanran Huang, Pengcheng Xiao, Juan Wang, Fan Wang, Wei Huang, Wenguo Cui, Ning Hu, Electroactive biomaterials regulate the electrophysiological microenvironment to promote bone and cartilage tissue regeneration, Adv. Funct. Mater. 23 (34) (2024) 2314079, https://doi.org/10.1002/adfm.202314079.
[42] T.U. Luu, W.F. Liu, Regulation of macrophages by extracellular matrix composition and adhesion geometry, Regen. Eng. Transl. Med. 4 (2018) 238–246, https://doi.org/10.1007/s40883-018-0065-z.